JGR Atmospheres

RESEARCH ARTICLE
10.1029/2023JD038610

Special Section:
Southern Ocean clouds, aerosols, precipitation and radiation

Key Points:

- The occurrence frequency of ice is greater in multi-layer clouds than in single-layer clouds
- Drop number size distributions are broader in multi-layer clouds compared to single-layer clouds
- Liquid drop number concentrations are approximately double in environments coupled with the surface compared to decoupled environments

Supporting Information:

Supporting Information may be found in the online version of this article.

Correspondence to:
J. J. D'Alessandro,
johndal@uw.edu

Citation:
D'Alessandro, J. J., McFarquhar, G. M., Stith, J. L., Diao, M., DeMott, P. J., McCluskey, C. S., et al. (2023). An evaluation of phase, aerosol-cloud interactions and microphysical properties of single- and multi-layer clouds over the Southern Ocean using in situ observations from SOCRATES. *Journal of Geophysical Research: Atmospheres*, *128*, e2023JD038610. https://doi.org/10.1029/2023JD038610

Received 1 FEB 2023
Accepted 9 JUL 2023

An Evaluation of Phase, Aerosol-Cloud Interactions and Microphysical Properties of Single- and Multi-Layer Clouds Over the Southern Ocean Using in Situ Observations From SOCRATES

John J. D'Alessandro[1,2,3], Greg M. McFarquhar[1,2], Jeffrey L. Stith[4], Minghui Diao[5], Paul J. DeMott[6], Christina S. McCluskey[7], Thomas C. J. Hill[6], Greg C. Roberts[8,9], and Kevin J. Sanchez[8]

[1]Cooperative Institute for Severe and High Impact Weather Research and Operations, University of Oklahoma, Norman, OK, USA, [2]School of Meteorology, University of Oklahoma, Norman, OK, USA, [3]Now at Department of Atmospheric Science, University of Washington, Seattle, WA, USA, [4]National Center for Atmospheric Research, Research Aviation Facility/Earth Observing Laboratory, Boulder, CO, USA, [5]Department of Meteorology and Climate Science, San Jose State University, San Jose, CA, USA, [6]Department of Atmospheric Science, Colorado State University, Fort Collins, CO, USA, [7]Climate and Global Dynamics Laboratory, National Center for Atmospheric Science, Boulder, CO, USA, [8]Scripps Institution of Oceanography, University of California San Diego, La Jolla, CA, USA, [9]Centre National de Recherches Météorologiques, Université de Toulouse, Météo-France, CNRS, Toulouse, France

Abstract Single- and multi-layer clouds are commonly observed over the Southern Ocean in varying synoptic settings, yet few studies have characterized and contrasted their properties. This study provides a statistical analysis of the microphysical properties of single- and multi-layer clouds using in-situ observations acquired during the Southern Ocean Cloud-Radiation Aerosol Transport Experimental Study. The relative frequencies of ice-containing samples (i.e., mixed and ice phase) for multi-layer clouds are 0.05–0.25 greater than for single-layer clouds, depending on cloud layer height. In multi-layer clouds, the lowest cloud layers have the highest ice-containing sample frequencies, which decrease with increasing cloud layer height up to the third highest cloud layer. This suggests a prominent seeder-feeder mechanism over the region. Ice nucleating particle (cloud condensation nuclei) concentrations are positively (negatively) correlated with ice-containing sample frequencies in select cases. Differences in microphysical properties are observed for single- and multi-layer clouds. Drop concentrations (size distributions) are greater (narrower) for single-layer clouds compared with the lowest multi-layer clouds. When differentiating cloud layers by top (single- and highest multi-layer clouds) and non-top layers (underlying multi-layer clouds), total particle size distributions (including liquid and ice) are similarly broader for non-top cloud layers. Additionally, drop concentrations in coupled environments are approximately double those in decoupled environments.

Plain Language Summary Weather and climate models continue to struggle simulating cloud microphysical properties over the Southern Ocean, including cloud phase occurrence frequencies. High resolution observations of Southern Ocean clouds are crucial toward improving model simulations. This paper uses in situ observations to compare and contrast microphysical properties and phase frequencies of single- and multi-layer clouds, as well as relates phase frequencies with ice nucleating particle and cloud condensation nuclei number concentrations. In situ observations used in this study were acquired during the Southern Ocean Cloud-Radiation Aerosol Transport Experimental Study. A suite of cloud probe instrumentation is used to classify 1 Hz cloud samples as either liquid, ice or mixed phase (i.e., liquid and ice particles in the same sample volume). The lowest occurrence frequency of liquid phase samples is observed in the lowest cloud layers of multi-layer clouds, whereas the highest frequency is observed in single-layer clouds. Ice nucleating particle number concentrations are negatively correlated with liquid phase occurrence frequencies in select cases. In contrast, cloud condensation nuclei number concentrations are positively correlated with liquid phase frequencies, although this is only observed for clouds above the boundary layer.

1. Introduction

Clouds over the Southern Ocean have been notoriously difficult to simulate in both climate models (e.g., D'Alessandro et al., 2019; Kay et al., 2012; Matus & L'Ecuyer, 2017; McCoy et al., 2014) and high resolution models (Huang et al., 2014, 2015; Naud et al., 2014). Climate models have overestimated shortwave absorption over this region (Trenberth & Fasullo, 2010), which has been attributed to the underestimation of liquid water content and cloud fraction (e.g., Bodas-Salcedo et al., 2016). This may be due in part to extremely low ice nucleating particle (INP) concentrations (N_{INP}) present over the Southern Ocean as observed from ships (McCluskey et al., 2018). While recent model changes have improved simulated clouds with an increased frequency of supercooled liquid, work is still required to further improve the representation of microphysical properties (e.g., Fiddes et al., 2022; Gettelman et al., 2020; McCoy et al., 2021; Yang et al., 2021) and the understanding of processes producing and sustaining supercooled water.

Single- and multi-layer clouds are commonly observed over the Southern Ocean, with prior observations indicating multi-layer clouds accounted for 34% of cases when clouds were present (Haynes et al., 2011). Multi-layer clouds refer to the presence of multiple cloud layers separated by a cloud free interstice, containing either precipitation or clear-sky (e.g., Intrieri et al., 2002; Liu et al., 2012). This is distinct from vertically heterogeneous clouds, in which cloud properties embedded within a single-cloud layer vary (e.g., Verlinde et al., 2013). Although climate models often fail to capture multi-layer clouds due to their coarse vertical resolution (e.g., Atlas et al., 2020), multi-layer clouds occur frequently and substantially impact the radiative budget. Because of this, climate models often parameterize vertical cloud overlap to adequately treat radiative fluxes throughout vertical columns (e.g., Collins, 2001).

Although the reasons that multi-layer clouds form is still uncertain, multiple explanations have been proposed. For example, Tsay and Jayaweera (1984) found that a combination of large-scale processes can account for multi-layered stratus. Herman and Goody (1976) showed that shortwave absorption by droplets within a cloud layer leads to evaporation within the cloud deck, which along with destabilization due to longwave cooling at cloud top can lead to the formation of two layers. Multiple cloud layers can also result from inhomogeneous temperature/moisture horizontal advection (Luo et al., 2008). They are also associated with additional complexities which do not need to be considered for single-layer regimes, such as seeder-feeder mechanisms (e.g., Fleishauer et al., 2002; Hobbs & Rangno, 1998; Houze, 2014).

Differences in cloud layering can impact the zonally averaged top-of-atmosphere longwave and shortwave radiative fluxes by the order of 10 W m^{-2} (Li et al., 2011), attributed in part to differences in the cloud layer heights and thicknesses. Further, overlying cloud layers can substantially impact the evolution of the underlying boundary layer clouds. Their presence increases downward longwave radiative flux by an average of 30 W m^{-2}, impacting turbulent mixing, vertical development and precipitation rates of the underlying cloud layers (Christensen et al., 2013).

Cloud layer microphysical properties substantially impact turbulent, precipitation and radiative properties. Thus, high vertical resolution measurements of cloud profiles are needed for both single- and multi-layer clouds. A few studies showing vertical profiles of cloud microphysical properties over the Southern Ocean using in situ observations have been performed (e.g., Ahn et al., 2017, 2018; Boers et al., 1996, 1998; Chubb et al., 2013, 2016). However, they were primarily case studies lacking statistically significant datasets, and they primarily focused on single-layer clouds. Little effort has been put toward contrasting the microphysical properties of single- versus multi-layer clouds, and the dearth of prior in situ observations over the Southern Ocean relative to the Arctic warrants a statistical analysis of the varying properties of single- and multi-layer clouds. Further, satellite observations are often restricted to cloud top (Coopman et al., 2020; Riedi et al., 2010), and there are uncertainties with low-level cloud retrievals due to attenuation (Hu et al., 2009) and low solar zenith angles (Khanal & Wang, 2018). For these reasons, in situ observations can be extremely beneficial toward analyzing both low-level cloud layers as well as multi-layered clouds commonly observed over this region.

This study aims to produce a statistical overview of single- and multi-layer clouds over the Southern Ocean using in situ observations. It extends the study of Schima et al. (2022) who used a combination of in-situ and remote sensing data to identify common features of the vertical cloud structure over the Southern Ocean, but who did not stratify clouds into single- or multi-layers, and who did not examine how cloud properties varied with the concentration of ice nucleating particles (INPs) or cloud condensation nuclei (CCN). The following section will describe the instrumentation and the methodology used to obtain vertical profiles as well as classify the measured profiles as either single- or multi-layer clouds. Section 3 presents the cloud microphysical properties and phase occurrence frequencies for single- and multi-layer clouds, as well as comparisons of CCN and INP in relation to cloud properties. Section 4 discusses the significance of the results presented in Section 3, and Section 5 delivers concluding remarks.

2. Methodology

2.1. Instrumentation and Cloud Presence/Phase Methodology

This study uses observations acquired with instruments onboard the National Science Foundation/National Center for Atmospheric Research Gulfstream-V (G-V) aircraft during the Southern Ocean Cloud-Radiation Aerosol Transport Experimental Study (SOCRATES). SOCRATES was based out of Hobart, Tasmania and consisted of 15 research flights. SOCRATES took place from 15 January to 28 February 2018, sampling the atmosphere over the Southern Ocean from 42° to 62°S and from 133° to 163°W. Flight plans were designed to ideally sample 10-min level legs above cloud, in cloud, and below cloud, followed by sawtooth legs (i.e., sawtooths) to obtain vertical profiles. A variety of synoptic conditions occurred during the campaign, including the passage of multiple extra tropical cyclones as well as an atmospheric river (1/28/2018, Finlon et al., 2020; Rauber et al., 2020). The aircraft primarily targeted cold sector boundary layer clouds, although regions of both synoptic ascent and descent were commonly sampled. Prevailing winds were primarily westerly and southwesterly. Additional details on synoptic conditions, flight objectives and analyses can be found in McFarquhar et al. (2021).

A suite of cloud probes and other instrumentation was installed on the G-V. The cloud droplet probe (CDP) is a single-scatter particle probe which gives information of cloud particle size distributions for particles with maximum dimension (hereafter size D) ranging from 2 to 50 μm. Because the CDP sizes particles assuming Mie theory which corresponds to diameters of spherical particles, there are large uncertainties in the derived particle sizes and mass contents for ice clouds. The two-dimensional stereo probe (2DS) is an optical imaging array probe with a photodiode array having a resolution of 10 μm from which particle number size distribution information can be derived. Although the width of the photodiode array of the 2DS corresponds to particles with maximum dimensions ranging from 10 to 1,280 μm, only particles having maximum dimension (D_{2DS}) greater than or equal to 50 μm were included in the derived particle number size distributions because of its small and highly uncertain depth of field for $D_{2DS} < 50$ μm (e.g., Baumgardner & Korolev, 1997). The SOCRATES 2DS size distributions and particle morphological data (Wu & McFarquhar, 2019) were determined using the University of Illinois/Oklahoma Optical Probe Processing Software (UIOOPS; McFarquhar et al., 2018; McFarquhar et al., 2017), and include corrections for removal of shattered artifacts (Field et al., 2003, 2006). Particles larger than the width of the photodiode array are included due to the use of particle reconstruction provided the particle center occurs within the array (Heymsfield & Parrish, 1978). Mass distribution functions are determined using the habit-dependent mass-size relationships summarized by Jackson et al. (2012, 2014) for the different particle habits that are identified in UIOOPS (McFarquhar et al., 2018) following a modified Holroyd (1987) approach. Hereafter, bulk properties of cloud particles measured by the CDP and 2DS correspond with the properties of cloud particles with D less than and greater than 50 μm, respectively.

Samples are determined to be either in-cloud or clear-sky following D'Alessandro et al. (2021), which utilizes measurements from the CDP and 2DS. Samples are considered in-cloud if the derived mass content of CDP observations (M_{CDP}) is greater than 10^{-3} g m^{-3} or if any particles are detected with $D_{2DS} > 50$ μm. These threshold values were selected to eliminate sea spray and other large aerosols. The low threshold of M_{CDP} ensures that even optically thin clouds are included in the sample. The phase of in-cloud samples is also determined following D'Alessandro et al. (2021), which determines the phase of small cloud particles ($D < 50$ μm) using a set of threshold values for the CDP and Rosemount Icing Detector measurements, whereas the phase of large particles ($D > 50$ μm) uses a combination of multinomial logistic regression and visual examination of particle imagery from the 2DS. The phase of large particles may be classified as either liquid, ice or mixed (i.e., a sample volume containing both liquid and ice particles) whereas the phase of small particles may only be classified as either liquid or ice. Number concentrations of the CDP (N_{CDP}) greater than 10 cm^{-3} are generally liquid samples (D'Alessandro et al., 2021; Finlon et al., 2019; Heymsfield et al., 2011; Lance et al., 2010). Additional information of the phase classification and associated uncertainties can be found in D'Alessandro et al. (2021).

Additional instrumentation to obtain measurements utilized in this study are described below. Filters were collected using a forward-facing inlet (Stith et al., 2009) on the G-V for offline immersion freezing measurements. INP number concentrations were determined from particles collected onto the filters and released into suspensions that were analyzed using the Colorado State University ice spectrometer (DeMott et al., 2017). The INP filter sample collection and analysis approach similarly follows that of previous aircraft studies (Levin et al., 2019; Twohy et al., 2016), wherein further details on the methodology can be found. Measurements of CCN were obtained using two miniaturized stream-wise thermal gradient CCN counters (Roberts & Nenes, 2005; Sanchez et al., 2021). One gathered 1 Hz data at a constant supersaturation of 0.43%, while the other operated with a scanning flow and temperature to measure CCN spectra from 0.06% to 0.87% supersaturation every 5 min. This study uses measurements from the latter, but only CCN data with supersaturations between 0.26% and 0.34%. This range of supersaturation is chosen since CCN concentrations at this range are similar to observed N_{CDP} concentrations (Sanchez et al., 2021). Shortwave irradiance measurements were taken with a Kipp and Zonen CMP22 Pyranometer. Infrared irradiance measurements were taken using two Kipp and Zonen CGR4 Pyrgeometers. Temperature was measured using a fast-response Rosemount temperature probe. For steady conditions the estimated accuracy and precision are 0.3 and 0.01 K, respectively. Water vapor was measured using the 25-Hz Vertical Cavity Surface Emitting Laser (VCSEL) hygrometer (Zondlo et al., 2010). Additional laboratory calibrations of the VCSEL water vapor measurements were conducted in summer 2018, and the final data were reprocessed (Diao, 2021). Relative humidity (RH) is calculated following Murphy and Koop (2005). The combined uncertainties from temperature and water vapor measurements results in the uncertainty of RH ranging from 6.3% to 6.7% from 17° to −31°C, respectively, which is the temperature range of the cloud layers in this study (discussed in more detail in the following section). Vertical air motion was measured with the Radome Gust Probe in combination with pitot tubes and the differential Global Positioning System. Cooper et al. (2016) reports a net uncertainty in the standard measurements of vertical wind to be 0.12 m s^{-1}, although this represents ideal sampling conditions. Additional information on the G-V gust probe performance and processing is provided in the manager's report (EOL, 2018; https://www.eol.ucar.edu/system/files/SOCRATES%20PM%20Report.pdf). Remote sensing platforms onboard the aircraft include the High-performance Instrumented Platform for Environmental Research (HIAPER) Cloud Radar (Vivekanandan et al., 2015) and High Spectral Resolution Lidar (Eloranta, 2006).

2.2. Cloud Layer Classification

Clouds measured during all sawtooth maneuvers, ascents and descents during SOCRATES are classified as either single- or multi-layer clouds. In the analysis, transects are first defined as ascending or descending legs, and included in the analysis provided the rate of altitude change was consistently greater than 3 m s^{-1} for the transect. The typical ascent or descent rate of the G-V during sawtooths was 5–7.5 m s^{-1}. Transects with vertical lengths less than 60 m are removed from this analysis, all of which only contained one single-cloud layer. Level legs are not included in the analysis because they do not provide information about the vertical profile.

An automated cloud layer classification method is introduced to provide an objective measure for identifying individual layers within each transect. For data obtained during each transect, a smoothing filter is applied to all 1-s in-cloud samples defined as having $M_{CDP} > 10^{-3}$ g m^{-3}. A binary array is first created (a cloud flag) where samples with $M_{CDP} > 10^{-3}$ g m^{-3} are set equal to one and all other samples equal to 0. A Savitzky-Golay smoothing method (Savitzky & Golay, 1964) is applied with a moving window of 30 1-Hz samples to each binary array. The Savitzky-Golay filter is used since it better preserves peak heights and widths of data features compared with lower order moving averages. Individual layers are identified where consecutive samples of the smoothed binary arrays exceed 0.5. Clear interstices between layers on the order of meters can potentially be captured using this method, with the exact threshold dependent on the aircraft rate of ascent or descent. The smallest distance between layers found here was 30 m. The vertical extent of the cloud layer within an area where the smoothed binary array exceeds 0.5 is determined to be between the highest and lowest in-cloud sample having $M_{CDP} > 10^{-2}$ g m^{-3}. The lower M_{CDP} threshold applied prior to smoothing ensures cloud top and base is contained in each area of the smoothed binary area exceeding 0.5. All layers identified using this method are shown by the shaded rectangles in Figure 1. The CDP is solely used to identify cloud layers without the use of the 2DS to ensure that the presence of precipitating ice or drizzle is not used to identify a cloud layer when small droplets or ice crystals are not present. A cloud layer is only included in the analysis if the entirety of the layer (cloud base to cloud top) is contained within the transect. Sensitivity tests were performed to determine how cloud top and base changed when the mass threshold was decreased to 10^{-3} g m^{-3} and increased to 0.05 g m^{-3} (not shown). Although the lower (higher) threshold increased (decreased) the total number of cloud layer samples by ~5% (~8%), the trends presented in the manuscript do not change regardless of the threshold used.

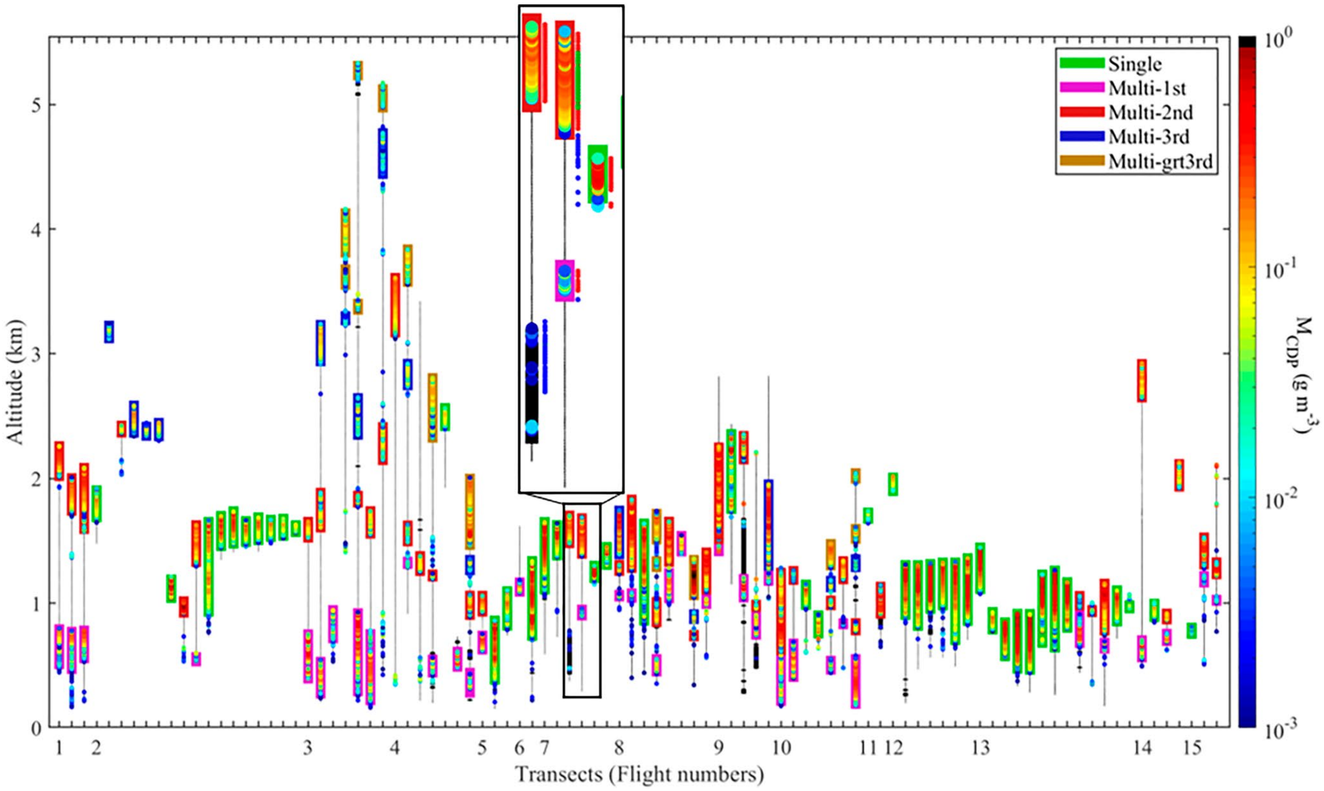

Figure 1. Vertical profiles of M_{CDP} from select sawtooths that meet criteria described in Section 2. Profiles are only shown for transects where the highest and lowest altitude samples of each transect are considered clear-sky. Colored circles show M_{CDP} where $M_{CDP} > 0.001$ g m^{-3}. Solid black lines show the vertical extent of each transect. Black shaded regions represent samples where $M_{2DS} > 0.01$ g m^{-3} and $M_{CDP} < 0.001$ g m^{-3}. Red, green and blue markers to the right of the transects in the magnified panel indicate liquid, mixed and ice phase samples, respectively. Phase markers are only shown for temperatures less than 0°C. Transects are from research flights which incrementally follow the flight numbers in the *x*-axis (e.g., all transects greater than or equal to 2 and less than 3 on the *x*-axis are from RF02). Note that cloud layers are slightly enlarged in order to encapsulate enlarged M_{CDP} markers.

Although flight plans were designed with the intent of sampling all cloud layers during sawtooth maneuvers, it is possible that some layers were missed if the G-V did not ascend or descend to the altitude where these layers were located. Furthermore, for transects where there was a very narrow interstice between layers, the irregular clustering of CDP measurements make it difficult to determine the number of layers. Thus, the G-V forward-facing camera was inspected for each transect to evaluate the classification. This was additionally required for cases when the G-V intersected the same cloud layer twice (e.g., protruding filaments of cloud below cloud base). Reflectivity profiles from the HIAPER cloud radar and retrievals from the HSRL acquired during the transects were similarly used to distinguish cloud layers and check for cloud layers directly above and below the aircraft. Manual inspection of the layer classification resulted in 16% of the layers requiring correction.

Figure 1 shows M_{CDP} from vertical transects flown by the G-V aircraft, with layers indicated by the coloring within each rectangular box. Each column represents a single-vertical transect, arranged in the order they took place as shown by the research flight number (RF01–RF15) underlying the respective columns. The color of the rectangular box surrounding the M_{CDP} shading represents the identification of that profile as either a single-layer, or the lowest (Multi-1st), second lowest (Multi-2nd), third lowest (Multi-3rd) or higher layer (Multi-grt3rd) in a multi-layer cloud as determined from the cloud layer classification. Both single- and multi-layer clouds were regularly encountered in approximately half the flights, whereas other flights predominantly sampled either multi-layer or single-layer clouds (e.g., RF01 only has two-layer clouds, RF12&13 primarily have single-layer clouds). The magnified panel in Figure 1 shows profiles representative of most of the layers sampled and includes phase information as colored markers immediately to the right of the transects. Cloud layers were typically composed of supercooled liquid and mixed phase samples. A case of light ice precipitation ($M_{2DS} < 0.01$ g m^{-3}) is observed for the highest cloud layer in the middle transect, indicated by the blue phase markers immediately to the right and underlying the top cloud layer. Cloud layers were often found to precipitate either supercooled drizzle or

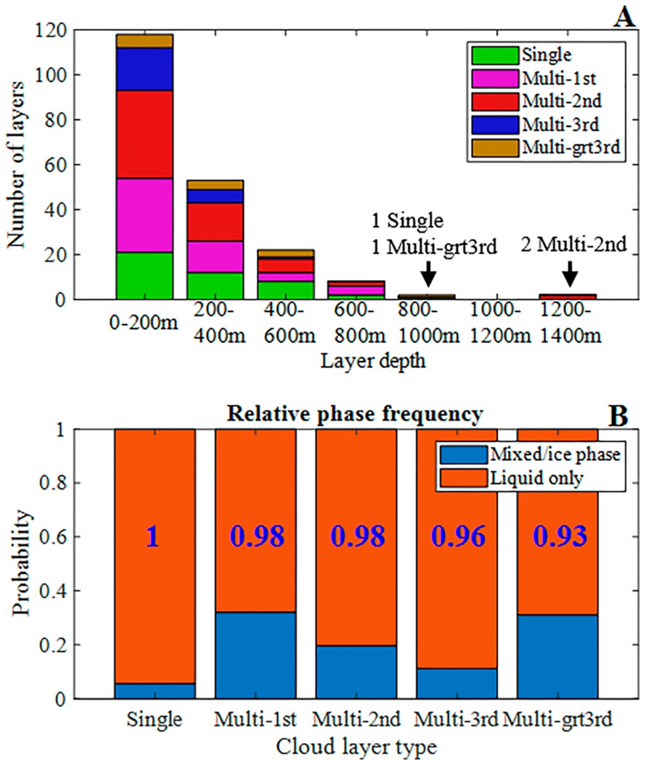

Figure 2. (a) A bar chart showing the number of cloud layers with given depth, sorted according to different cloud layer types. (b) Relative cloud phase frequency shown for different cloud layer types. Results in (b) are only shown at temperatures less than 0°C. The blue numbers are relative frequencies of the mixed phase to all ice-containing samples (mixed and ice phase). Results are only shown for sawtooths.

ice, which has been previously documented (Alexander et al., 2021; Schima et al., 2022). Overall, 55 single-layer clouds and 183 multi-layer clouds were identified from 153 transects using this procedure. Only 63% of the cloud layers obtained through the layer classification are shown in Figure 1, since Figure 1 only shows cloud layers from transects which do not have an in-cloud sample at the highest nor lowest point. Although cloud layers are included in the analysis regardless of their altitude, the vast majority of sampling took place below 3 km (96% of single-layer clouds and 98% of multi-layer clouds).

Since M_{CDP} is solely used to determine in-cloud conditions, the cloud layer classification method fails to capture ice cloud layers with M_{CDP} below the in-cloud threshold. One such layer is in the magnified panel of Figure 1 as seen by the presence of $M_{\mathrm{2DS}} > 0.01$ g m^{-3} (black shading and blue markers). Note that the phase information is only visible for approximately half the length of the layer since temperatures exceed 0°C below the markers and phase information is only provided for temperatures less than 0°C. There were six such layers in total (2% of the observed layers), which are not included in the analysis to be consistent with the in-cloud definition ($M_{\mathrm{CDP}} > 10^{-3}$ g m^{-3}) proposed to exclude precipitating particles. Additionally, the cloud layer classification method may fail to accurately capture cloud layers which contain ice layers embedded within multiple liquid or mixed phase layers. However, there were only three such layers (1% of the layers) embedded with multiple liquid layers as well as ice layers which were deep enough to prevent the smoothing algorithm from adequately classify the cloud layers. These layers were not included in the analysis.

3. Results

3.1. Cloud Layer Overview

Figure 2 shows the number of profiles with different layer depths (i.e., geometric thickness) for the single- and multi-layered cases (Figure 2a), as well as the normalized occurrence frequency of different phases that occur in single-layer and multi-layer clouds (Figure 2b). The number of Multi-2nd layers (70) is greater than the number of Multi-1st (64) layers because every sawtooth does not necessarily capture every cloud layer within a given atmospheric profile. Figure 2a shows that relatively thin cloud layers with depths <200 m are more frequent than deeper layers for both single-layer and multi-layer clouds, and for all different layers of the multi-layer clouds, with these thin cloud layers representing 59% of the layers sampled during SOCRATES. Cloud layers with average temperatures less than 0°C make up 76% of all the layers sampled, with 63% of all such layers having depths <200 m. Here cloud layers above and within the boundary layer are explored separately due to inherent differences in air properties and aerosol profiles at these heights. Approximately 72% of the multi-layer clouds were observed within the boundary layer and 28% above the boundary layer, and approximately 70% of single layer clouds were observed within the boundary layer. The boundary layer heights were determined from dropsonde data using a maximum gradient method developed by Hande et al. (2012) where boundary layer heights are determined as the altitude where the maximum gradient of virtual potential temperature occurs. The range of possible heights is restricted to 100 and 2,500 m, and the virtual potential temperature is smoothed with a five-point moving average. Other methods have been proposed for determining boundary layer heights using alternative gradient methods utilizing other parameters (e.g., Engeln & Teixeira, 2013) or using a bulk Richardson number (Seidel et al., 2012; Vogelezang & Holtslag, 1996) where the boundary layer height is the lowest altitude where the bulk Richardson number exceeds 0.25. From visual inspection, it was determined that the maximum gradient method produces better estimates of the boundary layer height than the bulk Richardson method, possibly because the Richardson method is only a measure of local turbulence, which may not be suitable for convective boundary layers. The mean and median boundary layer heights using the maximum gradient method are both ∼1,450 m with a standard deviation of 510 m. For flights without dropsonde data (dates 1/15, 2/3, 2/4), boundary layer heights are estimated via visual inspection from in situ temperature measurements acquired during sawtooths. Finally, boundary layer heights are interpolated using a nearest neighbor method over each respective flight. Some layers could therefore be incorrectly characterized as either above or within the boundary layer based on uncertainties or limitations associated with the interpolation method.

Figure 2b shows that single-layer clouds contain the smallest percentage of ice-containing samples (6%), where ice-containing samples are either ice-phase or mixed-phase clouds, whereas the lowest layers of multi-layer clouds have the highest observed frequency of ice-containing phases (32%). The frequency incrementally decreases with increasing multi-layer cloud height up to the third lowest cloud layer. The highest layers of multi-layer clouds have nearly similar frequencies of ice-containing samples (31%) as the lowest layers. The phase frequencies are separately analyzed for above and within the boundary layer (not shown), and the trends discussed above are observed in both cases (i.e., greatest liquid phase frequencies in single layer clouds, lowest liquid phase frequencies in lowest multi-layer clouds and increasing liquid phase frequencies up to the third highest cloud layers). Frequency values within the boundary layer are all within 10% of those in Figure 2b, whereas values are much more variable above the boundary layer. The fraction of samples that are mixed-phase compared to all ice-containing samples is greatest for single-layer clouds, with slightly lower frequencies for multi-layer clouds, with the frequency decreasing with increasing cloud height (blue text within respective columns of Figure 2b). Within all cloud layers, over 95% of ice-containing samples are mixed-phase showing the dominance of supercooled water regardless of layering.

The vertical distances and properties between the layers of multi-layer clouds are also explored in an effort to document differences in dynamical and precipitation characteristics. The frequency distribution of distances between cloud layers is shown in Figure 3a. The distances are skewed to the left, with approximately half less than 200 m and a median distance of 209 m. A wide variety of synoptic conditions were sampled during SOCRATES, with winds primarily westerly (∼270°) or southwesterly (∼220°). Figure 3b shows that winds were primarily southwesterly for closely residing cloud layers (i.e., distance between layers less than 200 m), whereas they were primarily westerly for other multi-layer clouds, suggesting a dynamical link for multi-layer clouds with varying distances in-between the layers.

Normalized frequency distributions of RH between cloud layers in Figure 3c show the air was often nearly saturated between all cloud layers, with peak occurrence frequencies of 90%–95%. These peaks are greater for closely residing cloud layers (∼0.2) compared with layers further apart (∼0.1). To explore whether this is related to the presence of in-cloud samples within the layers, clear-sky frequencies (number of clear-sky samples to all samples) and liquid phase frequencies (number of liquid phase samples to all phases) are shown in Figure 3d for temperatures from −20° to 0°C, which contained 99% of samples for depths less than 200 m and 95% for depths greater than 200 m. To determine the fraction of in-cloud samples that are precipitating, the clear-sky and liquid phase frequencies are computed using only in-cloud samples that contain particles with $D > 50$ μm. The clear-sky frequencies vary from ∼0.7 to 0.95 for depths exceeding 200 m and 0.4–0.7 for depths less than 200 m. The relatively high clear-sky frequencies may not necessarily indicate the top cloud layer never was precipitating, since the aircraft may have penetrated the layers after the event. However, the clear-sky frequencies are lowest from −5° to 0°C for closely residing cloud layers, with over half of the samples within the layers associated with precipitation. This is also the temperature range which contains half of all closely residing cloud layer samples.

The liquid phase frequencies of the precipitating samples vary from 0.25 to 0.75 for depths less than 200 m and 0.05–0.45 for depths exceeding 200 m. The lowest liquid phase frequencies are observed in the highest temperature bin consistent with precipitating ice beneath liquid topped cloud layers. The liquid phase frequency from −20° to 0°C for both depth ranges is approximately 0.32, highlighting a higher frequency of ice-containing samples relative to liquid-only samples.

3.1.1. INP Related to Cloud Phase

Determining the concentration of INP over the SO is difficult in part due to their relatively sparse concentrations over the region (McCluskey et al., 2018; McFarquhar et al., 2021), which means long averaging times are required to get statistically significant samples. The following discussion provides context for the INP observations gathered from the G-V aircraft during SOCRATES and used in this analysis. It is worth noting that these observations are the first airborne INP measurements taken over the Southern Ocean region. Sampling of INP is taken over continuous durations on the order of minutes, which here are defined as sample areas. To accommodate the low aerosol loadings over the Southern Ocean, filters were collected during periods (i.e., within given sample

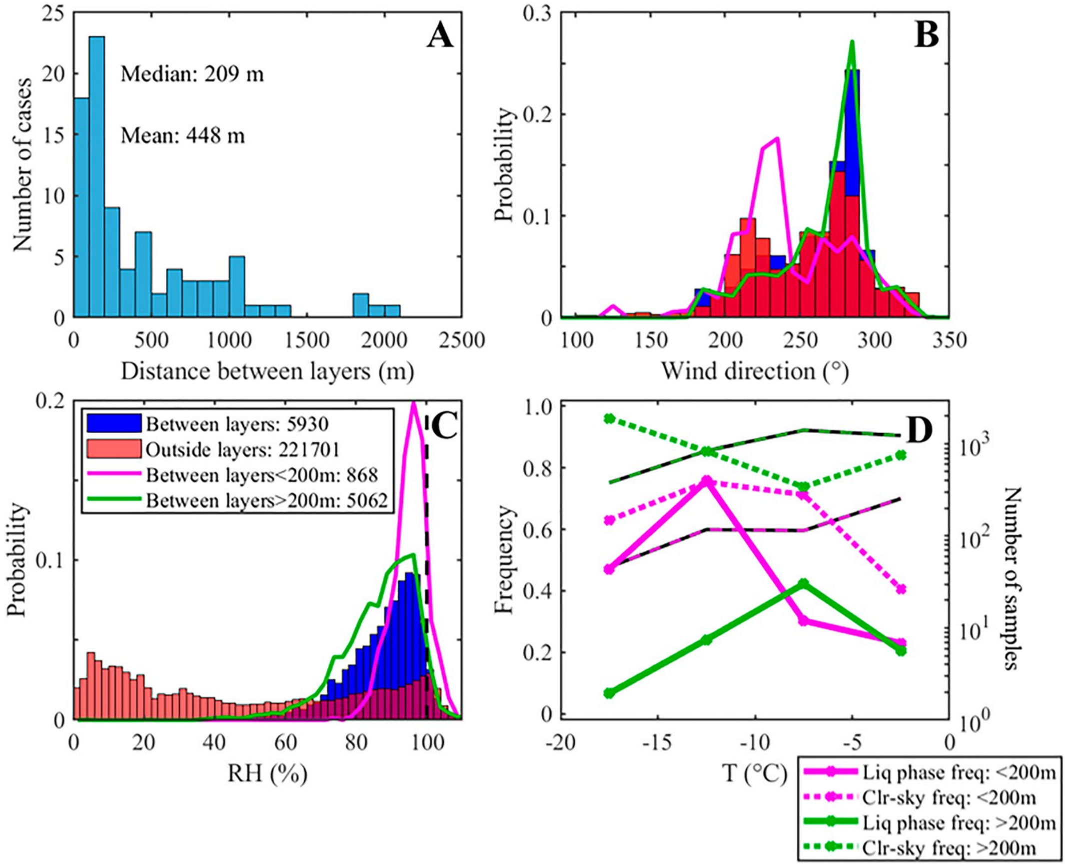

Figure 3. (a) Histogram of depth lengths in between cloud layers. The mean and median depth lengths are shown in the panel. (b) Normalized frequency distributions of wind direction for different conditions. The legend in C applies to subsets here, and the sample size of the subsets is provided in the legend. The purple (green) line represents the distribution of samples within cloud layers where the depth is less than (more than) 200 m. The outside layer includes all samples from the northbound portion of the research flights, excluding samples between and within cloud layers, as well as samples lower than the lowest altitude of samples within layers (<450 m). (c) Normalized frequency distributions of relative humidity. Subsets of distributions are similar to those in (b). (d) Liquid phase (solid line) and clear-sky (dashed line) relative frequencies of samples in between layers binned in 5°C temperature intervals. Results are similarly restricted to depths less than and greater than 200 m as in (b and c). The black and purple (green) dashed line shows the number of samples for depths less (greater) than 200 m (right ordinate).

areas) of clear-air that were representative of the below-cloud layer, above-cloud layer and in the free troposphere. The sample areas were often combined in post-campaign processing accounting for flow rates which ranged from a few to 13 L per minute (depending on altitude). Sample areas above and within the boundary layer were separately combined, with the combined areas spanning up to 15° latitude. This resulted in accumulated sample volumes ranging from 129 to 840 standard liters of air per flight. The total data acquisition time of all samples amounts to approximately 23 hr, with a total of 32 filter samples obtained. Since the reported activation temperatures vary for different combined sample areas, reported N_{INP} are averaged at 1°C intervals to obtain N_{INP} with a constant activation temperature resolution of 1°C.

The following analysis relates N_{INP} with relative phase frequencies. To obtain adequate cloud phase sample size(s), combined INP sample areas are interpolated using a nearest neighbor method over the respective flights. Cloud phase data within the interpolated sample areas (including sawtooth and level-leg data) is then related to $\mathrm{N_{INP}}$ from the same sample area(s). The interpolation is separately performed for sample areas above the boundary layer and within the boundary. This mostly results in interpolated sample areas derived from single sample areas above and within the boundary layer spanning the entire research flights, with the exception of research flights 1, 3, 4, 10. Namely, with the exception of the research flights listed, all in-cloud data above (within) the boundary layer is related with a single set of reported $\mathrm{N_{INP}}$ above (within) the boundary layer.

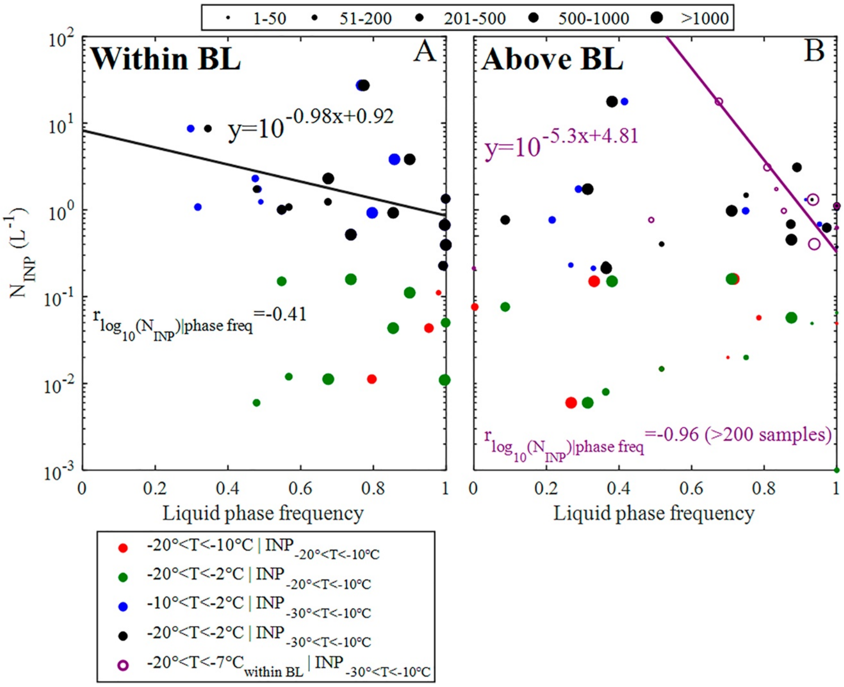

Figure 4. Scatterplots of N_{INP} related to liquid phase frequency (i.e., the frequency of liquid phase samples relative to all in-cloud samples) for samples within the boundary layer (a) and above the boundary layer (b). Samples are taken within the interpolated ice nucleating particle (INP) sample areas as described in the text. Different colored markers show liquid phase frequencies taken within specified temperature ranges compared with N_{INP} having different ranges of activation temperatures. The purple circles compare phase frequencies within the boundary layer to N_{INP} above the boundary layer using the above boundary layer interpolated area. Best fit lines and correlations correspond to the respective phase frequency and INP activation temperature ranges. The size of the data points represents the number of in-cloud samples associated with a given data point (i.e., the number of in-cloud samples within a specified temperature range located within a given interpolated sample area).

Scatterplots relating N_{INP} and liquid phase frequency are shown in Figure 4. Results are separately shown within the boundary layer (Figure 4a) and above the boundary layer (Figure 4b). The different colored markers denote cases where the liquid phase frequency is taken within a specified temperature range (left-hand side of legend text) located within a given interpolated sample area and relates it to N_{INP} having activation temperatures within a specified range (right-hand side of legend text) associated with the same interpolated sample area. The N_{INP} values over the specified activation temperature ranges are the sums of the averaged N_{INP} values determined for the constant 1°C activation temperature bins. Measurements of INP are reported with activation temperatures ranging from −30° to −10°C, noting $\mathrm{N_{INP}}$ is only measurable for activation temperatures <−10°C. Phase data for temperatures below −20°C are not included because D'Alessandro et al. (2021) previously showed there is a sharp decrease in supercooled liquid below −20°C, with ~93% of samples between −30° and −20°C being ice phase. Strong negative relationships would likely indicate a prevalence of primary nucleation over the region. Perhaps the most likely temperature range and N_{INP} activation temperature range expected to show such relationships would be those having similar ranges. However, data points representing liquid phase frequencies from −20° to −10°C and N_{INP} with activation temperatures in the same range (red points) are associated with low sample sizes (i.e., number of in-cloud samples). This is observed with only three data points within the boundary layer, and seven above the boundary layer (three of which have sample sizes less than 200; denoted by marker size). This is due in part to the fact that the number of in-cloud samples from −10° to 0°C is more than a factor of two greater than the number of samples from −20° to −10°C (D'Alessandro et al., 2021); N_{INP} have their lowest concentrations at relatively higher activation temperatures which increase semi-exponentially with decreasing activation temperatures (Järvinen et al., 2022).

There are a few N_{INP} ranges which capture negative relationships between liquid phase frequency and N_{INP} associated with primary nucleation. One is for N_{INP} with activation temperatures from −30° to −10°C within the boundary layer, where the correlation between N_{INP} and liquid phase frequencies from −20° to −2°C is −0.41.

This negative correlation may be related to the fact that INP measurements below −20°C are more reliable, and thus may better reflect N_{INP} having higher activation temperatures. The correlation is similar (−0.51 to −0.41) when decreasing the range of activation temperatures toward those greater than −30°C, until activation temperatures exceed −25°C (not shown). However, this negative correlation is only observed within the boundary layer, which is unexpected since there were no in-cloud samples obtained below −20°C within the boundary layer. Therefore, the correlation may be related to sedimenting INP from above the boundary layer even though there is no notable relationship between similar N_{INP} and liquid phase frequency temperature ranges above the boundary layer. One possible explanation for this observation may be the prominence of efficient ice nucleation due to pre-activated INP (Mossop, 1956), whereby localized regions above the boundary layer may only experience significant primary nucleation via pre-activated INP. Thus, primary ice nucleation may occur at lower temperatures above the boundary layer, and contributions from alternative processes such as accretion and seeding mechanisms may decrease liquid phase frequencies at higher temperatures underlying the localized areas. There is indirect evidence for this when relating N_{INP} above the boundary layer with phase frequencies within the boundary layer (Figure 4b; purple circles). This is done by obtaining the phase frequencies below the boundary layer using the above boundary layer interpolated sample areas. A correlation of −0.96 is observed between N_{INP} with activation temperatures from −30° to −20°C and phase frequencies from −20° to −7°C for datapoints exceeding 200 samples, and a correlation of −0.87 is observed by removing the only datapoint with less than 200 samples having a liquid phase frequency of ~0.5. This finding is not directly indicative of a significant contribution from pre-activated INP, as results may also be indicative of a seeding mechanism resulting from INP which are not pre-activated. Further, it is important to note that to the authors' knowledge there are no prevailing studies which similarly suggest the importance of pre-activated INP in any region globally.

All the other N_{INP} ranges are weakly correlated with liquid phase frequency ($|r| < 0.2$), with the exception of N_{INP} with activation temperatures from −20° to −10°C and liquid phase frequencies within the same temperature range within the boundary layer, although this data set only contains three points. Aside from select combinations of N_{INP} and phase frequencies discussed above, there are no clear relationships between most combinations of the listed phase frequencies and N_{INP}, suggesting a prominence of alternative ice initiation/growth processes (secondary ice nucleation, accretion, etc.). Relationships may be sensitive to whether INP sampling took place above or below clouds, although it is at best extremely difficult to incorporate this distinction due to the interpolated sampling area method discussed above. Additionally, results may be sensitive to the fact that N_{INP} values in Figure 4 are biased toward reported N_{INP} at the lowest end of their respective activation temperature ranges, due to the semi-exponential increase in reported N_{INP} with decreasing activation temperatures. At the very least, results here provide a benchmark analysis toward directly relating INP to the frequency of ice over the Southern Ocean.

3.1.2. CCN Related to Cloud Phase

Liquid phase frequencies are also related to CCN number concentrations (N_{CCN}) to determine the potential impacts of CCN on cloud phase. Due to the greater spatial resolution of CCN measurements compared with INP sample areas, a method is derived to obtain a CCN number concentration associated with each cloud sample. Since droplet shattering on the community aerosol inlet of the CCN counter introduces error in its measurements (Hudson & Frisbie, 1991), CCN measurements cannot be used within in-cloud samples. To avoid such errors, suitable CCN concentration measurements (hereafter referred to as N_{CCN}) are determined using a moving window ±n seconds (n ranges from 100 to 500 s) from each cloud sample. Within this window, the average N_{CCN} is calculated only using clear-sky samples. The averaging method is also restricted to samples above or within the boundary layer, depending on the location of the in-cloud sample. Thus, each in-cloud sample is associated with a "background CCN concentration" value based on the moving window average. Results applying this methodology are shown in Figure 5, showing the liquid phase frequency for different temperature ranges (where temperature values are used at the in-cloud location) above the boundary layer (Figures 5a–5c) and within the boundary layer (Figures 5d–5f). The different color lines denote the liquid phase frequencies for different terciles of N_{CCN}, where the red line denotes samples in the lower tercile, the black line in the middle tercile and the blue line in the upper tercile. Terciles are determined within the respective temperature bins, whereas terciles determined over the entire temperature range (−20° to 0°C) are shown in the respective panels. Each column shows results using a different moving average window size (100, 250 and 500 s), shown overlying the respective columns. Results are relatively consistent over the different window sizes but not location. Within the boundary layer, liquid phase frequencies are either relatively constant or slightly increase with decreasing temperature for all the moving window sizes (Figures 5d–5f). The possible exception is the lower tercile at smaller windows, with

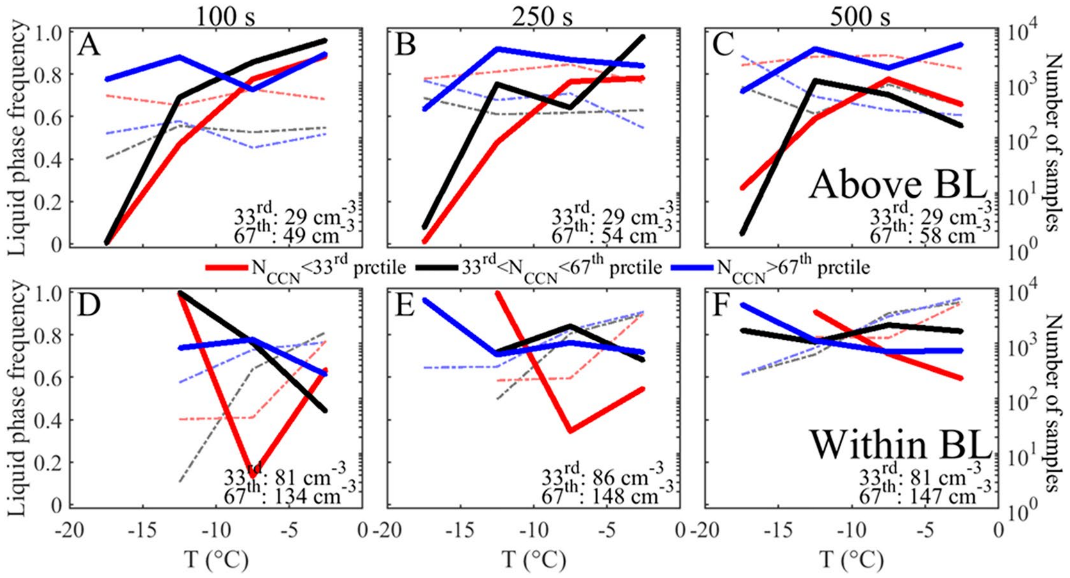

Figure 5. Liquid phase frequencies within 5°C temperature bins above (a–c) and within (d–f) the boundary layer for different N_{CCN} terciles. A "background cloud condensation nuclei (CCN) concentration" (N_{CCN}) is determined for each in-cloud sample by averaging the CCN concentration measurements over the clear-sky samples within a window of $\pm n$ seconds from each in-cloud sample. Results are shown for different moving window sizes, which are shown overlying each respective column. Temperatures are from the location of the respective in-cloud samples. Frequencies are determined for different ranges of average N_{CCN} (shown by the colored lines). Average N_{CCN} terciles are calculated within the respective temperature bins, whereas terciles calculated over the entire temperature range are included in the respective panels. The number of in-cloud samples are denoted by the dotted-dashed lines.

an initially low liquid phase frequency from −10° to −5°C which increases with increasing window size as the sample size increases. Although inconsistent with observed increases in the frequency of ice-containing cloud samples with decreasing temperatures (D'Alessandro et al., 2021), results here are consistent with the increasing liquid phase frequencies with increasing cloud height (Figure 2b). In contrast, most liquid phase frequencies generally decrease with temperature over all the CCN percentiles above the boundary layer (Figures 5a–5c). Stark contrasts in the liquid phase frequencies above the boundary layer are observed for the different CCN percentiles which were not observed within the boundary layer. Namely, liquid phase frequencies are much greater within high N_{CCN} environments than low N_{CCN} environments at temperatures less than −10°C. In fact, with the exception of one temperature bin (from −10° to −5°C for the ±100 s window; Figure 5a), the liquid phase frequencies in the high N_{CCN} environments are greater than the low N_{CCN} environments for all temperatures and moving window sizes. Liquid phase frequencies for the middle tercile do not always lie between the upper and lower terciles, and are often closer to frequencies of the lower terciles at temperatures less than −10°C. This suggests relatively high CCN perturbations may be required to maintain the absence of ice at these relatively lower temperatures. Previous studies have found high N_{CCN} environments correspond with increased frequencies of supercooled liquid in low-level Arctic clouds, which has been suggested to be due to increasing lifetimes of supercooled liquid clouds (Filioglou et al., 2019). Alternatively, varying N_{CCN} environments may be representative of different air mass source regions, and differences in phase frequencies may be the result of the different aerosol sources. Sanchez et al. (2021) identified four aerosol regimes sampled during SOCRATES, and found environments with high N_{CCN} commonly originated or passed over the Antarctic coast, where elevated phytoplankton biomass (relative to the open ocean) is a major contributor of biogenic emissions (Sanchez et al., 2016). Additional explanation(s) may be related to varying secondary ice production mechanisms related to the presence of large droplets, which would be limited in a high N_{CCN} environment. For example, drops having maximum dimensions exceeding ~50 μm have been observed to eject small ice particles as they freeze (i.e., droplet fragmentation), primarily at temperatures less than −10°C (Korolev & Leisner, 2020). However, Järvinen et al. (2022) found little evidence to suggest this is a prominent secondary ice production mechanism over the SOCRATES region. A more prominent mechanism is referred to as the Hallett-Mossop process, which is characterized by splintering of small ice particles off of graupel during riming (Hallett & Mossop, 1974). Previous studies have noted its likely presence over

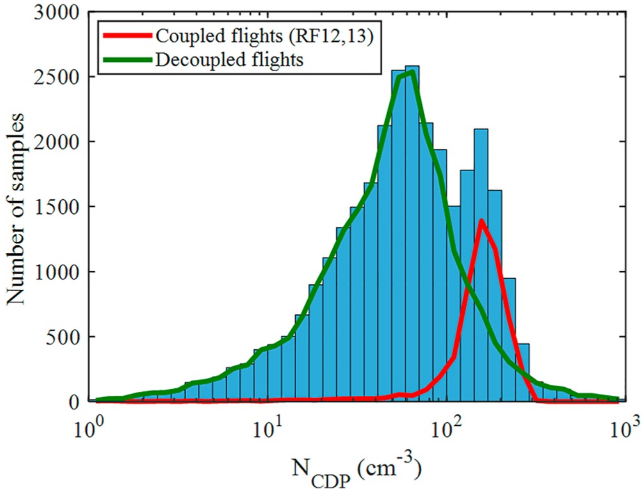

Figure 6. Frequency distribution of N_{CDP} for in-cloud conditions for all flights (blue bars). Green and red lines show distributions of N_{CDP} for decoupled and coupled environments, respectively. Results here include level periods and sawtooths.

the Southern Ocean (Huang et al., 2021; Järvinen et al., 2022), although this process is primarily restricted to temperatures from −8° to −3°C where the greatest liquid phase frequency differences are not observed.

An analysis comparing differences in drop concentrations in decoupled and coupled environments is provided in Figure 6. Results separated in this manner can provide insight into how surface-sourced parameters impact drop concentrations (e.g., sea spray acting as CCN). Most of the boundary layers were decoupled with the exception of RF12 and RF13, where the presence of coupling was determined using the dropsonde data following (Z. Wang et al., 2016). Figure 6 shows a distinct bimodality in N_{CDP} due to differences of N_{CDP} in the coupled and decoupled environments. The mode of N_{CDP} for decoupled flights is 70 cm^{-3} and for coupled flights 160 cm^{-3}, consistent with high aerosol number concentrations emitted from the ocean serving as effective CCN in the coupled cases. Perhaps unexpectedly, average N_{CCN} within the boundary layer is not the highest for either of the coupled research flights, but rather is highest for RF09 (191 cm^{-3}), second highest for RF12 (175 cm^{-3}) and the third highest for RF13 and RF08 (both are 136 cm^{-3}). Furthermore, average N_{CCN} for RF12&13 above the boundary layer were the fifth and sixth highest of all 15 research flights. The tendency for RF12&13 not having the highest average N_{CCN} is similarly observed when evaluating N_{CCN} at supersaturations greater than and less than 0.3% (not shown). This is indicative of higher updraft speeds associated with these two flights, which is consistent with a less kurtotic distribution of vertical air motions (kurtosis = 4.2) observed for in-cloud observations from these flights compared to the other research flights (kurtosis = 10.3; not shown). Note that kurtosis is used to capture the tail ends of distributions (greater updraft and downdraft speeds) rather than skewness which may not capture the greater updraft speeds if greater downdraft speeds are also present. However, Sanchez et al. (2021) suggested that recent particle formation above the boundary layer and particle growth/processing within the boundary layer are the primary source(s) of CCN in this region. Alternatively, lower drop concentrations associated with decoupled flights could be related to greater entrainment-mixing or precipitation scavenging.

3.2. Cloud Layer Properties and Profiles of Radiative Fluxes and Drop Clustering

Figure 7 shows normalized frequency distributions of N_{CDP}, M_{CDP}, the standard deviation of D from CDP drop size distributions (σ_{CDP}) and the mean volume weighted diameter (MVD$_{CDP}$) for single-layer clouds and the different layers of multi-layer clouds using data from all flights. In Figure 7a it is seen that the N_{CDP} mode for single-layer clouds is greater than 10^2 cm^{-3}, coinciding with the N_{CDP} mode for flights taken in coupled environments shown in Figure 6 (RF12 and RF13, both of which primarily sampled single-layer clouds as seen in Figure 1). To examine the effect of coupling on the distribution of $N_{CDP,}$ results for single-layer cases restricted to decoupled environments are separately shown by the dashed line. When comparing the solid and dashed black lines for the properties in all panels, N_{CDP} is the only property shown that significantly diverges for the coupled and decoupled environments. N_{CDP} distributions in single-layer decoupled environments are more similar to distributions of multi-layer clouds than to single-layer cloud distributions in coupled environments. In contrast, the modes for M$_{CDP}$, σ$_{CDP}$ and MVD$_{CDP}$ are relatively similar in coupled and decoupled environments (all of which are between 0.1 and 0.3 g m^{-3}, 3–4 and ∼16 μm, respectively).

When comparing single-to multi-layer cases, single-layer cases are slightly skewed to larger M_{CDP} values, whereas both σ$_{CDP}$ and MVD$_{CDP}$ (Figures 7c and 7d) are skewed to larger values for multi-layer cases. These results suggest multi-layer clouds observed during SOCRATES had less liquid water content than single-layer cases, but broader droplet distributions and larger mean particle sizes. The significance of these differences is tested using Mann-Whitney U-Tests and Kolmogorov-Smirnoff tests. Mann-Whitney U-test determines whether the median of one distribution is significantly greater or less than the other, whereas the two-sample Kolmogorov-Smirnov test determines the significance of the maximum absolute difference between the two cumulative frequency distributions, both of which use lookup tables. These tests do not require prior knowledge of the distributions' shapes. Every test comparing single-layer and the varying multi-layer types' M_{CDP}, σ_{CDP} and MVD$_{CDP}$ rejects the

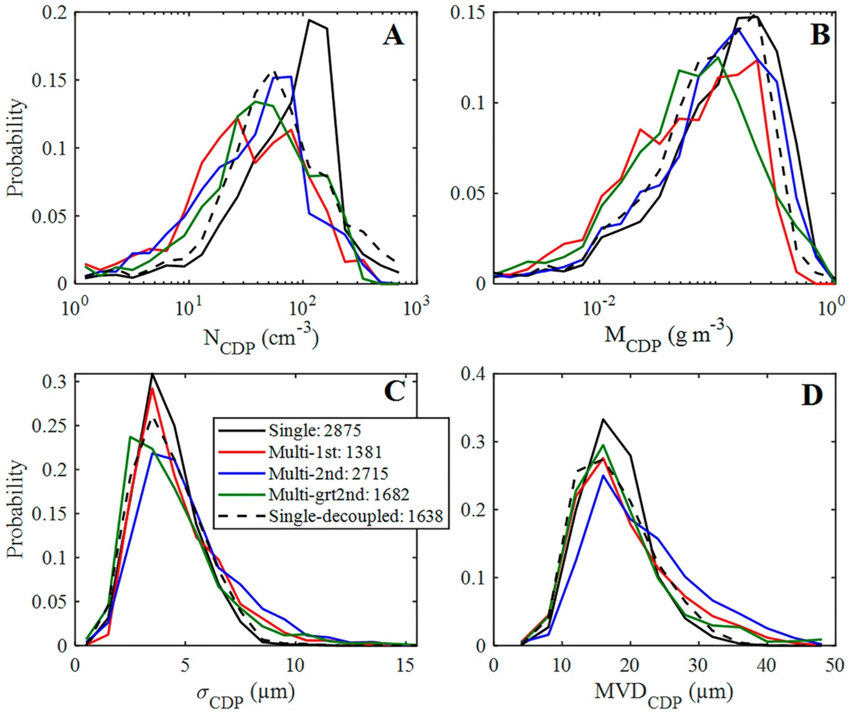

Figure 7. Normalized probability distributions of N_{CDP} (a), M_{CDP} (b), σ_{CDP} (c) and $\mathrm{MVD}_{\mathrm{CDP}}$ (d) for different cloud layer types. The black solid and dashed lines show all single-layer samples and single-layer samples from decoupled environments, respectively. The number of samples for each layer type is shown in the legend. Results are only shown for sawtooths.

null hypothesis that both sample sets are taken from the same population at a significance level of 10%. These tests were similarly performed for only liquid phase samples to test whether differences are related to the relative phase distributions of liquid and mixed phase samples. For example, available liquid in mixed phase samples may be partitioned to large ice particles which often exceed sizes detectable by the CDP (directly impacting M_{CDP}). However, with the exception of σ_{CDP} in Multi-1st, all the tests reject the null hypothesis, signifying differences in M_{CDP}, σ_{CDP} and $\mathrm{MVD}_{\mathrm{CDP}}$ for the different cloud types are not related to cloud phase.

Parameters in Figure 7 are also separately evaluated within and above the boundary layer for single- and multi-layered clouds in Figure 8 to determine if significant differences exist. Note the relatively low sample size of single-layer samples above the boundary layer might contribute to the multi-modal distributions for N_{CDP} and $\mathrm{MVD}_{\mathrm{CDP}}$, although uncertainties associated with the interpolated boundary layer height may be significant as well. Distributions of N_{CDP} and M_{CDP} are shifted toward larger values for multi-layered clouds within the boundary layer, consistent with higher N_{CCN} within the boundary layer. Although distributions of σ_{CDP} and $\mathrm{MVD}_{\mathrm{CDP}}$ appear similar for both multi-layer cloud cases, Mann-Whitney U-tests and Kolmogorov-Smirnov tests reject the null hypothesis that both sample sets are taken from the same population at a significance level of 10%. Overall, distributions of σ_{CDP} and $\mathrm{MVD}_{\mathrm{CDP}}$ are more positively skewed for both multi-layer cases compared with the single layer cases, confirming differences in the different cloud types is unrelated to differences in boundary layer and free tropospheric conditions.

It is crucial to examine how the properties vary in relation to their location within the cloud layer to get insight into physical processes occurring in the clouds and impacts on vertical profiles of radiative heating. Figure 9 shows joint histograms of both shortwave (solar) and longwave (terrestrial) irradiance as a function of the normalized height within a cloud layer, defined following McFarquhar et al. (2007) as

$$z_n = \frac{(z - z_{\mathrm{Cloud\_base}})}{(z_{\mathrm{Cloud\_top}} - z_{\mathrm{Cloud\_base}})} \tag{1}$$

where z refers to the altitude of the local 1 Hz sample, $z_{\mathrm{Cloud\_top}}$ and $z_{\mathrm{Cloud\_base}}$ refer to the altitudes of cloud top and cloud base for a particular layer, respectively (i.e., the highest and lowest samples within a layer having

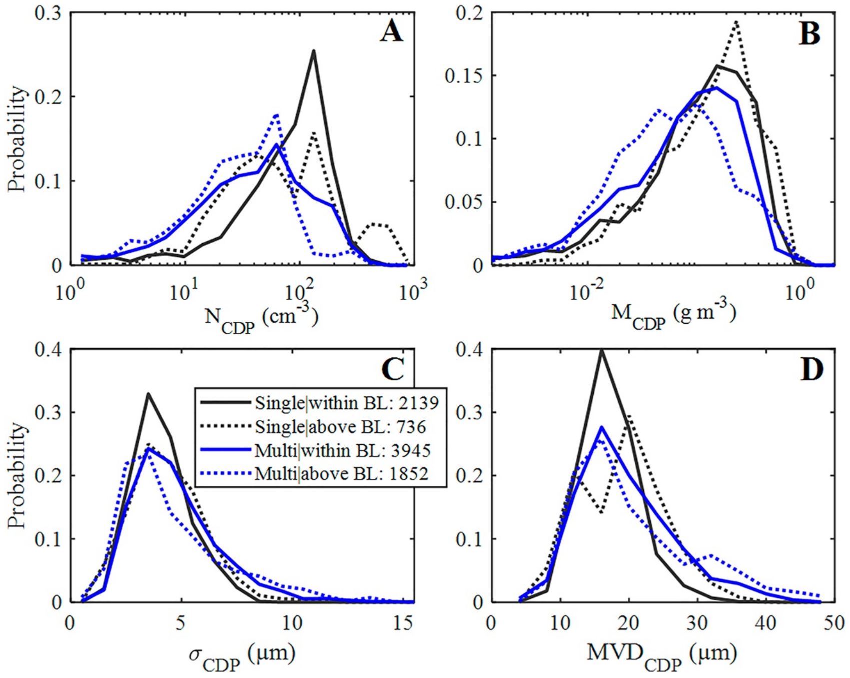

Figure 8. Similar to Figure 7, except single- and multi-layer cloud properties are separately evaluated for samples above the boundary layer and within the boundary layer.

$M_{CDP} > 0.01$ g m^{-3}). Cloud layers are split into two categories: those that are the highest layer of their respective regime (top cloud layers; Figures 9a–9c) and those that are underlying another cloud layer (non-top cloud layers; Figures 9d–9f). Layers in the non-top category are only associated with multi-layer clouds and should receive less solar radiation than top layers. This is precisely what is observed when comparing the solar irradiance (F_{solar}) in Figures 9a and 9d: most measurements in the top cloud-layers occur between 400 and 600 W m^{-2} at $z_n > 0.9$

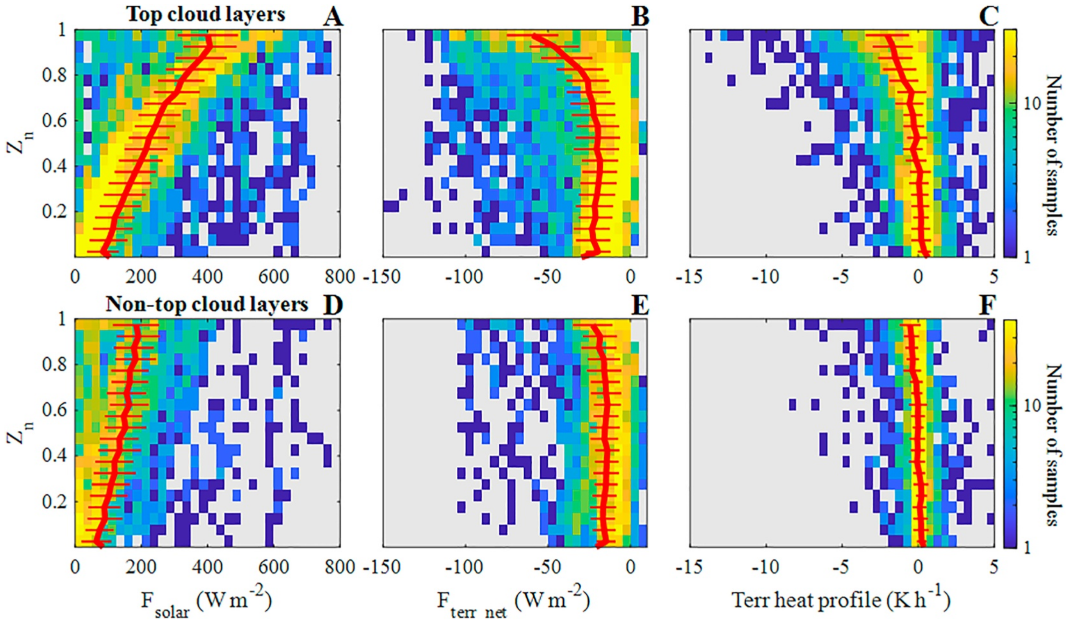

Figure 9. Joint histograms showing the frequency of downwelling solar irradiance (F_{solar}; (a and d), net terrestrial irradiance (F_{terr_net}; (b and e) and associated heating profiles from terrestrial irradiance (c and f) as a function of z_n for layers including single-layer and the highest layer of multi-layer clouds (top cloud layers; a–c) and for underlying cloud layers (non-top cloud layers; (d–f). Vertical red lines show average irradiance and heating rates and horizontal lines denote standard deviations.

whereas there are nearly zero (<∼10) cases of solar irradiance greater than 400 W m^{-2} for the non-top cloud layer. Likewise, most measurements of net longwave irradiance ($F_{\mathrm{terr\_net}}$) ranges from -110–0 W m^{-2} for the top cloud layer at $z_n > 0.9$, with a mean value of −50 W m^{-2}. In contrast, there are nearly zero cases of $F_{\mathrm{terr\_net}} < -50$ W m^{-2} for non-top cloud layers.

The heating profiles shown in Figures 9c and 9f reveal relatively weak cloud top cooling associated with longwave radiation for both the top and non-top layers. The terrestrial heating rate is computed as

$$\frac{\partial T}{\partial t} = -\frac{1}{\sum_{\mathrm{i}=1}^{3} \rho_{\mathrm{i}} C_{p,i}} \frac{\mathrm{d}F_{\mathrm{terr\_net}}}{\mathrm{d}z} \tag{2}$$

where T is temperature, t is time, z is vertical distance, ρ_{i} is the total density of the air, liquid or ice mass, and $C_{p,i}$ is the specific heat of either air, water or ice at constant pressure (Braslau & Dave, 1975; Petty, 2006). In mixed phase samples, the specific heat of water at constant pressure is used for the entire cloud mass since efforts are not made to derive the cloud mass separately for the ice or liquid phase (therefore there are only two iterations in the summation). However, exchanging it for the specific heat of ice at constant pressure is inconsequential to the results as the air density is significantly greater than that of the cloud mass. Average cooling rates are ∼0.5 K hr^{-1} at $z_n > 0.9$ for non-top cloud layers, and lower than ∼2.5 K hr^{-1} for top cloud layers. Such low cooling rates are associated with emitted longwave radiation from overlying cloud layers for non-top cloud layers, as well as relatively low mass contents of clouds over this region, as seen with M_{CDP} having modes ranging from 0.1 to 0.2 g m^{-3} for all cloud layer types (Figure 7b). Weaker cooling rates may result in weaker cloud top turbulent mixing for non-top cloud layers, resulting in different lifetimes or evolutions for different cloud layer regimes. Higher cooling rates are associated with greater average liquid mass of the top cloud layers. Specifically, average cloud top cooling rates are 1.5 K hr^{-1} greater for cloud layers with average $\mathrm{M}_{\mathrm{CDP}}$ above the 50th percentile (0.2 g m^{-3}) than below the 50th percentile (not shown).

The clustering of droplets, which can have implications for many factors such as precipitation onset (Shaw et al., 1998) and the evolution of raindrop size distributions (McFarquhar, 2004), is evaluated using joint histograms in Figures 10a and 10b and Figures 10c and 10d for all top cloud layers and all non-top cloud layers, respectively. The clustering index (CI) is a commonly used metric (e.g., B. A. Baker, 1992; Chaumat & Brenguier, 2001; Jaczewski & Malinowski, 2005) that is defined as

$$\mathrm{CI} = \left(\frac{V}{M} - 1\right) \tag{3}$$

where M is the mean and V is the variance of a given parameter over a given number of samples. This metric takes advantage of the fact that a Poisson distribution has an equal mean and variance. By subtracting 1 from V/M, a droplet distribution sampled from a population with a constant mean rate results in CI equaling 0 cm^{-3} (in the case of drop concentrations per cubic centimeter), and CI increases with increasing droplet heterogeneity. Note that CI less than 0 cm^{-3} ($V < M$) is simply characterized as underdispersed (i.e., having a variance lower than that expected for a Poisson distribution). In this study, CI is calculated every second using 10 Hz observations, providing a measure of inhomogeneity over scales of ∼120 m (depending on flight speed). In order to scale results on a logarithmic scale, the subtraction of 1 is removed from Equation 2 so all results have a minimum possible value greater than 0 cm^{-3}. The altered calculation (i.e., altered CI; ACI) used in this study is given by

$$\mathrm{ACI} = \log_{10}\left(\frac{V}{M}\right) \tag{4}$$

Figures 10a and 10c show ACI for N_{CDP} ($\mathrm{ACI}_{\mathrm{N\_CDP}}$), whereas Figures 10b and 10d show ACI for M_{CDP} ($\mathrm{ACI}_{\mathrm{M\_CDP}}$). Joint histograms of $\mathrm{ACI}_{\mathrm{N\_CDP}}$ are relatively similar for layers from $0 < z_n < 0.8$, with most values between −0.4 and 0.2 cm^{-3}. Near cloud base ($z_n = 0$), $\mathrm{ACI}_{\mathrm{N\_CDP}}$ varies from ∼0 to 1 cm^{-3} and average values are slightly greater than those from $0.2 < z_n < 0.8$. Values increase near cloud top, with most $\mathrm{ACI}_{\mathrm{N\_CDP}}$ between 0.5 and 2 cm^{-3}. Increased droplet clustering has previously been found to occur at cloud top, which has been attributed to mixing and cloud top entrainment in the past (B. A. Baker, 1992; Dodson & Small Griswold, 2019; Small & Chuang, 2008).

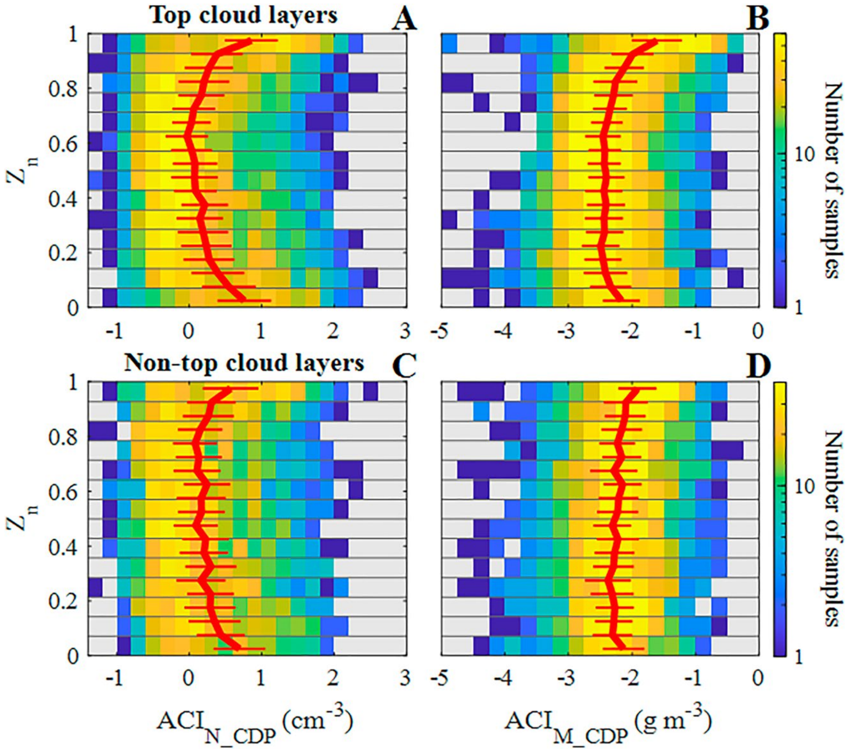

Figure 10. Joint histograms shown with ACI_{N_CDP} (a and c) and ACI_{M_CDP} (b and d). The red vertical lines show average ACI_{N_CDP} and ACI_{M_CDP} and the horizontal lines denote standard deviations.

Discernible differences in clustering at cloud top are observed between the top and non-top layers near cloud top, which are likely due to differences in entrainment and/or mixing strength. Namely, average ACI_{N_CDP} and ACI_{M_CDP} are greater at cloud top for the top cloud layers compared with non-top layers. The most notable differences are observed for ACI_{M_CDP}, where the greatest occurrence frequencies exceed ACI_{M_CDP} equal to -1 g m^{-3} only for the top cloud layers. In addition, the variability of ACI_{M_CDP} between cloud top and the underlying cloud is greater for top cloud layers than for non-top layers. These indicators of greater entrainment and/or mixing (e.g., greater clustering values) are expected with greater cooling rates at the top of top cloud layers compared with non-top cloud layers (Figures 9c and 9f).

Other factors may account for the small-scale variability of N_{CDP} and M_{CDP} at cloud top, such as previously observed generating cells (Y. Wang et al., 2020) or upsidence waves (i.e., gravity waves visible within a cloud deck) (Rahn & Garreaud, 2010). The influence of large-scale factors on ACI_{N_CDP} is evaluated in Figure 11, which shows level leg cloud top observations from two research flights. Satellite imagery for both cases reveal undulations in cloud cover surrounding the two transect regions, although cirrus immediately overly the flight path for RF13 (not shown). The Brunt-Vaisala frequency for both cases is determined (using ambient virtual potential temperature) from nearby sawtooths and is 0.016 rad s^{-1} and 0.027 rad s^{-1} for RF06 and RF13, respectively. These values suggest both environments are conducive for upsidence waves, and are consistent with the lengths of the wavelike structures observed for N_{CDP}. Namely, that the wavelength is longer for RF06 (~15 km; Figure 11a) than for RF13 (~2 km; Figure 11b). Autocorrelations of N_{CDP} for RF06 (Figure 11c) and RF13 (Figure 11d) capture the wavelike structures of N_{CDP}, having peak autocorrelation values above the bands of rejection at lags of 15 km for RF06 and at ~2, 4.5 and 7 km for RF13. Jiang and Wang (2012) found evidence that liquid water content increases in the regions of upward motion from upsidence waves. A similar analysis is performed for both cases using M_{CDP} and a similar wavelike structure and autocorrelation is found for RF06, although not for RF13 (not shown).

For both cases, ACI_{N_CDP} does not possess the wavelike structures observed for N_{CDP}, which is observed when applying autocorrelations to ACI_{N_CDP}. A wavelike structure in ACI_{N_CDP} appears in RF06, but most amplitudes

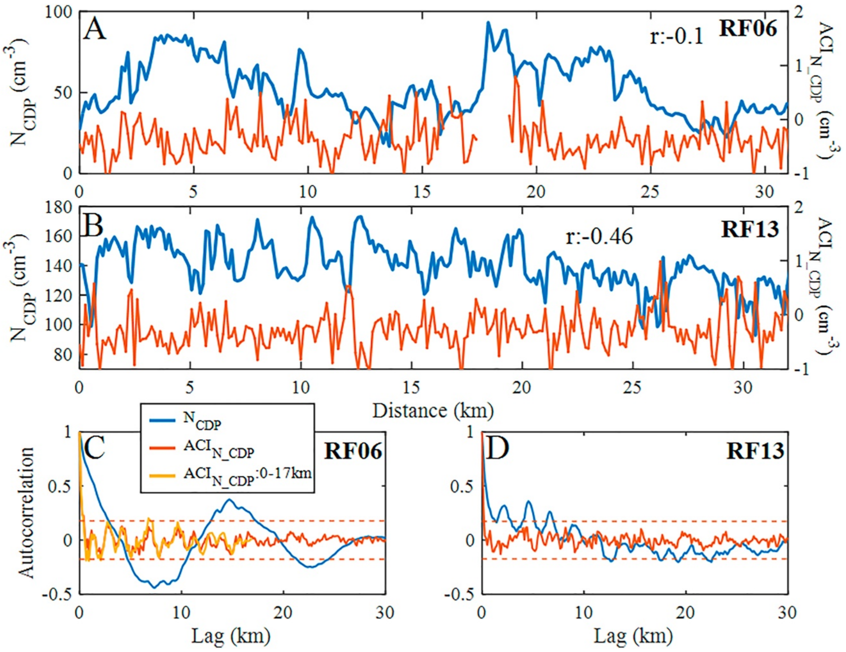

Figure 11. Two time series of level legs taken at cloud top showing N_{CDP} (blue) and ACI_{N_CDP} (red) from RF06 (01:47:00 to 01:51:55 UTC; (a)) and RF13 (02:19:00 to 02:24:00 UTC; (b)). Correlations are included in the respective panels. Autocorrelations of N_{CDP} and ACI_{N_CDP} are shown for RF06 (c) and RF13 (d). Bands for rejection testing each autocorrelation = 0 under the assumption of white noise are shown as dashed lines, which are provided at the 95th percentiles. Autocorrelations are determined for flight data interpolated onto a 1D grid with a constant incrementally increasing distance (lag) of 130 m, based on the average flight speed for both cases (~130 m s^{-1}). The autocorrelation of ACI_{N_CDP} from 0 to 17 km is also provided for RF06, due to missing data from ~17.5 to 19 km (missing data is also observed at ~16 km, but the interpolation method captures the fine scale variability).

do not exceed the significance bounds. In contrast, autocorrelations exceed the significance bounds for N_{CDP} at lags comparable to the observed wavelengths (e.g., a 15 km wavelength where peak N_{CDP} are observed at ~5 ± 2 km and 20 ± 3 km for RF06). Correlations of N_{CDP} and ACI_{N_CDP} are −0.10 and −0.46 for RF06 and RF13, respectively. Increases in ACI_{N_CDP} often correspond with decreases in N_{CDP} (e.g., at 2.5 and 12 km for RF13, Figure 11b), consistent with trends expected from entrainment-mixing.

Average normalized cloud particle size distributions, such that the integrated concentration equals one, are shown in Figure 12. Specifically, normalized size distributions are obtained by weighting number concentrations of the respective bins by the total cloud particle concentration. Distributions include contributions from both the CDP and 2DS and are normalized over their combined range (2–1,280 μm). To characterize their height variation, normalized particle size distributions are first interpolated to a 2D grid with z_n spaced over 0.01 intervals. Additionally, normalized particle size distributions are interpolated to the 2D grid over 80 logarithmically scaled bins ranging from 2 to 1,280 μm. Results are then smoothed using a two-dimensional convolution and a 3 × 3 box kernel (i.e., averaging kernel). This method is analogous to that commonly used in image smoothing (Kim & Casper, 2013), allowing for a clear visual depiction of particle size distributions over the range of z_n. Focusing on the top cloud layers (Figure 12a), the maximum normalized $N(\log(D))$ (i.e., $dN/d\log(D)$) > 0.01 at $z_n < 0.1$ occurs at D from 2 to 20 μm. These maximum $N(\log(D))$ shift toward larger sizes with increasing z_n. At $z_n > 0.6$, maximum normalized $N(\log(D)) > 0.05$) occur at D from approximately 10 to 30 μm. This shift is consistent with droplet activation occurring near cloud base producing small droplets, which grow with increasing height due to condensational growth and collision-coalescence.

There are notable differences for the non-top cloud layers (Figure 12d) compared to the top cloud layers (Figure 12a). The non-top layers have greater small droplet concentrations at $z_n > 0.4$ compared to the top layers with normalized $N(\log(D))$ at $D < 10$ μm being ~0.05 throughout the entire cloud depth, whereas values at $D < 10$ μm decrease well below 0.01 for $z_n > 0.5$ in top cloud layers (green shading). Further, $N(\log(D))$ greater than 0.01 reach sizes up to 40 μm throughout most of the cloud for non-top cloud layers. This is not seen for the

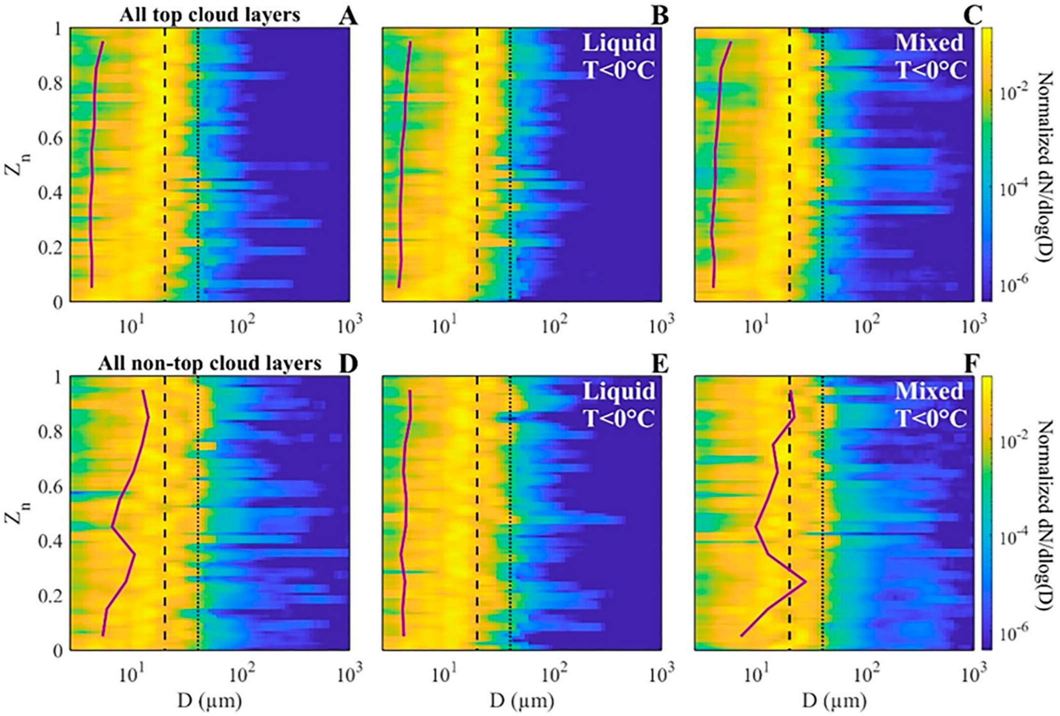

Figure 12. Normalized size distribution functions combining cloud droplet probe and 2DS observations are averaged over z_n, using an image smoothing method outlined in the text. The top (bottom) row shows results for top (non-top) cloud layers. Results are shown for all in-cloud samples in the left column (a and d), liquid phase samples at temperatures less than 0°C in the middle column (b and e) and for mixed phase samples in the right column (c and f). Purple lines show the average standard deviation of particle size over the entire size distributions, applied prior to the convolution. The dashed and dotted lines correspond with $D = 20$ μm and $D = 40$ μm, respectively.

top cloud layers throughout most of the cloud. These trends highlight the differences seen in Figures 7c and 7d, namely that non-top cloud layers which only occur in multi-layer clouds have broader droplet size distributions. These broader distributions contain larger relative frequencies of both smaller ($D < 10$ μm) and larger (D from 30 to 50 μm) drops. Purple lines show the average σ of D for the normalized size distributions, and these values are larger for non-top cloud layers compared to top cloud layers over the entire depth. Normalized $N(\log(D))$ at $D > 50$ μm are also greater for the non-top cloud layers throughout the cloud depth.

Broader distributions are likely related to a greater frequency of mixed phase samples within non-top cloud layers, which may be associated with a broader range of ice crystals. This is suggested by plotting results separately for liquid phase samples (Figures 12b and 12e) and mixed phase samples (Figures 12c and 12f); normalized values of $D > 10^2$ μm are clearly greater for the mixed phase samples of both top- and non-top cloud layers compared with liquid phase samples. However, differences in cloud phase frequency do not account for all the observed differences between the layer types. Non-top cloud layers still have broader drop size distributions ($D < 50$ μm) than top cloud layers regardless of the cloud phase, which is likely due to particle interactions occurring vertically through local cloud layers. This is confirmed by computing average σ_{CDP} within the vertical profile, which shows values are ~0.5 μm greater for liquid phase samples and ~1.5 μm greater for mixed phase samples in non-top cloud layers at $z_n > 0.5$ (not shown). In fact, average ice concentrations in mixed phase samples with maximum dimensions exceed 200 μm (aspherical $N_{\mathrm{2DS\_D>200\mu m}}$) are nearly an order of magnitude greater in non-top cloud layers (1.7 L^{-1}) than top layers (0.2 L^{-1}). The average σ are much lower for mixed phase samples in the top cloud layers compared with non-top layers. This is due to mixed phase samples in the top cloud layers having much greater drop concentrations (average $N_{\mathrm{CDP}} = 120\ \mathrm{cm}^{-3}$) than non-top cloud layers (average $N_{\mathrm{CDP}} = 40\ \mathrm{cm}^{-3}$). Similarly, drop concentrations are greater in the top layers for liquid phase samples as well (average $N_{\mathrm{CDP}} = 110\ \mathrm{cm}^{-3}$) than non-top layers (average $N_{\mathrm{CDP}} = 70\ \mathrm{cm}^{-3}$), consistent with the lowest N_{CDP} observed for the lowest cloud layers in Figure 7a. The higher concentrations in top cloud layers are observed even when removing samples from coupled environments, which causes the average N_{CDP} of top layers to decrease ~10 cm^{-3} for both phases.

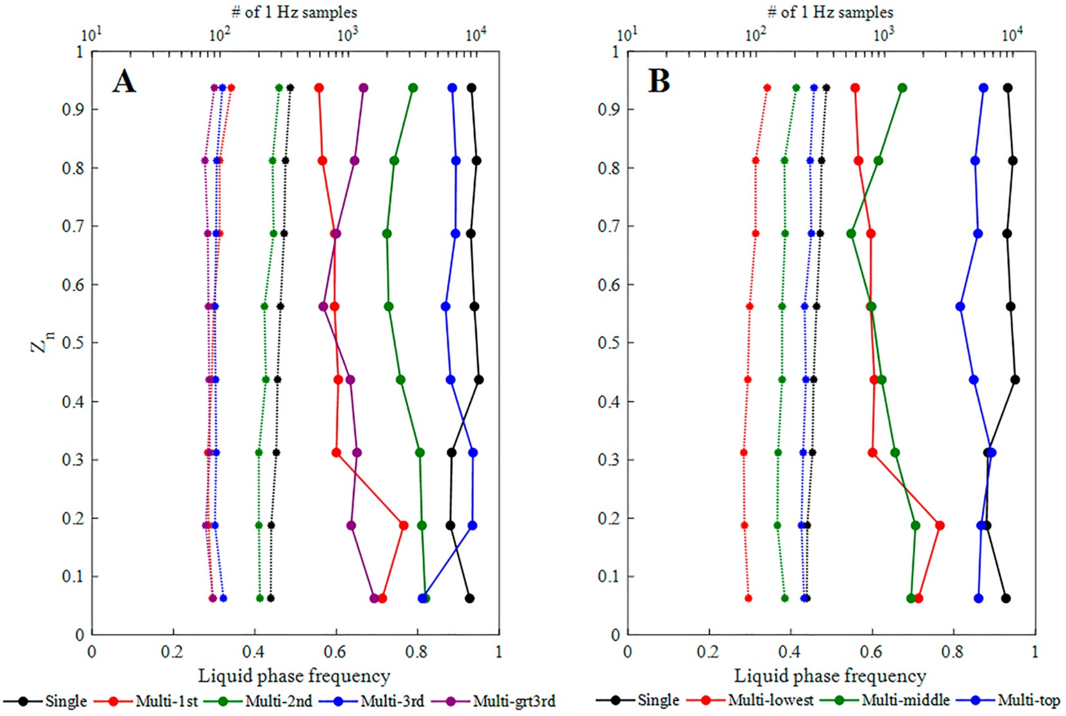

Figure 13. Cloud phase frequency as a function of z_n (solid lines) colored according to the cloud layer for single-layer and multi-layer clouds, where ordering of multi-layer height is characterized by incremental order from the lowest layer (a) and by whether layers are the lowest, highest, or middle layer (b). Dotted lines show the number of samples for respective cloud layers following the top abscissa. Results are restricted to temperatures less than 0°C.

3.3. Vertical Distributions of Phase and Average Cloud Properties

In addition to characterizing multi-layer clouds based on the relative height within the cloud layer and based on whether in the top or non-top cloud layer, the relative frequency of liquid phase with respect to z_n is shown in Figure 13. Results for multi-layer clouds are sorted by cloud height relative to the lowest cloud layer (as in Figures 2 and 7; left panel) or by the lowest, middle and highest layers (right panel). Results for the lowest cloud layers (Multi-1st and Multi-lowest) are the same for both categorizations. Single-layer clouds are seen to contain the most liquid phase samples, which is consistent with Figure 2b. Furthermore, the liquid phase frequency is lowest for $z_n < 0.4$, which is similar to previous findings that Arctic single-layer mixed phase clouds contain the highest frequency of ice particles in the lower half of the cloud (McFarquhar et al., 2007; Mioche et al., 2017). The lowest cloud layers in multi-layer clouds have much lower liquid phase frequencies than in single-layer cases (consistent with Figure 2b), with liquid phase frequencies decreasing from 0.75 to 0.60 from cloud base to cloud top.

For multi-layer clouds, the second and third highest layers (Multi-2nd and Multi-3rd, respectively; Figure 13a) have liquid frequencies varying between 0.75 and 0.95 throughout the normalized heights. Cloud layers overlying the third highest layers have lower liquid phase frequencies which are comparable to the lowest cloud layers, varying from 0.55 to 0.70 throughout their depth. These layers typically occur at lower temperatures. Figure 13b shows results discriminating multi-layer clouds into the highest (Multi-top) and layers residing between the highest and lowest cloud layers (Multi-middle). The middle layers have much lower liquid phase frequencies compared with the top cloud layers. In fact, the liquid phase frequencies are comparable between the middle and lowest layers, whereas the highest cloud layers have liquid phase frequencies comparable to single-layers. Note that Multi-grt3 has frequencies resembling middle layers rather than the top layers, because top layers are heavily weighted by cases where there are only two cloud layers in the atmospheric column. The phase frequency structure of multi-layer clouds is consistent with what would be expected from a prominent seeder-feeder mechanism. Primary nucleation may occur at the highest cloud layers where temperatures are lowest, of which 61% were between −10° and 0°C and 78% between −20° and 0°C. Low liquid frequencies at the top of the lowest cloud layers may indicate seeding from above.

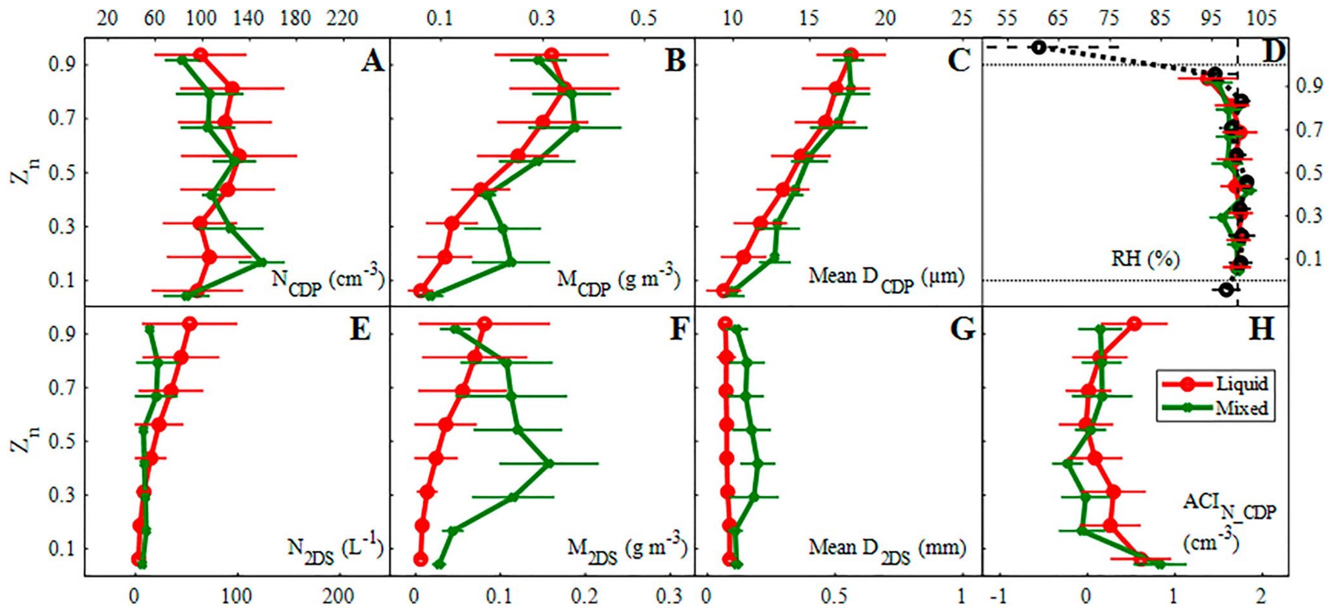

Figure 14. Averaged N_{CDP} (a), M_{CDP} (b), Mean D_{CDP} (c), relative humidity (RH) (d), N_{2DS} (e), M_{2DS} (f), Mean D_{2DS} (g) and ACI_{N_CDP} (h) as function of z_n for single-layer cloud regimes. Horizontal lines are standard deviations. Results are shown for liquid phase samples with the red lines and mixed phase samples with the green lines. Properties are averaged within z_n bin sizes of 0.125. All panels show results for z_n between 0 and 1 except for RH (d), which includes additional bins above and below the cloud (dashed lines). Black circles in RH denote clear-sky samples. Note error bars for the liquid phase in G are smaller than most of the data points.

The remainder of the findings address how other microphysical properties vary as a function of z_n for the different layers, whose sample sizes are found in Figure 13. Figure 14 shows vertical profiles for single-layer clouds. Results are separately shown for liquid and mixed phase samples by the red and green lines, respectively. Ice phase samples are not included due to the relatively small sample size of ice phase compared with mixed phase samples (e.g., blue text in Figure 2b). The top row shows N_{CDP}, M_{CDP} and number weighted mean diameter reported by the CDP (Mean D_{CDP}) (Figures 14a–14c). All of these variables, with the exception of N_{CDP} for mixed phase samples, increase with height. The discussion for the remainder of this section focuses on liquid phase samples due to (a) the small sample size of mixed phase observations for all cloud layers and (b) the fact that such observations do not necessarily represent a secondary vertical structure, because the majority of mixed phase samples were embedded within primarily liquid phase cloud layers.

Figures 14e–14g shows vertical profiles for the properties of particles with dimensions greater than 50 µm (N_{2DS}, M_{2DS} and Mean D_{2DS}). Both N_{2DS} and M_{2DS} increase with z_n, whereas Mean D_{2DS} decreases with z_n. Note that M_{2DS} and Mean D_{2DS} are larger for mixed phase throughout most of the cloud depth, consistent with the coexistence of larger particles which are primarily ice. Mixed phase Mean D_{2DS} were separately determined for spherical and non-spherical particles greater than 200 µm, and Mean D_{2DS} for non-spherical particles were greater than spherical particles at all z_n (not shown). Figure 14h shows ACI_{N_CDP}, which has a U-shaped distribution similar to Figures 10a and 10c meaning that maximum ACI_{N_CDP} are at cloud base and cloud top. Vertical profiles of RH in Figure 14d are ~100% throughout the cloud depth, with a deviation of ~95% at cloud top. Black dots with dashed lines show RH for clear-sky regions which primarily occur above cloud top ($z_n > 1.0$). Since the layer classification allows for clear-sky samples to exist within a profile, such samples (although very few) may also occur within a cloud layer ($0 < z_n < 1$). The analysis of RH is also shown above cloud top and below cloud base ($z_n > 1$ and $z_n < 0$, respectively). Above cloud top and below cloud base data is simply the neighboring 1 Hz clear-sky samples to the respective cloud edges. Clear-sky samples below cloud base are nearly saturated, whereas clear-sky samples above cloud top have an average RH of 60%, with significant variability (standard deviation of ~25%).

Figure 15 shows vertical profiles for the lowest cloud layer in multi-layer clouds. Similar to single-layers, M_{CDP}, Mean D_{CDP}, and N_{2DS} all increase with height. Average ACI_{N_CDP} and Mean D_{2DS} have similar distributions, with peak values near cloud top and cloud base for ACI_{N_CDP} and decreasing values with height for Mean D_{2DS}. Differences between the cloud layer types are primarily observed for N_{CDP} and RH, where N_{CDP} roughly decreases

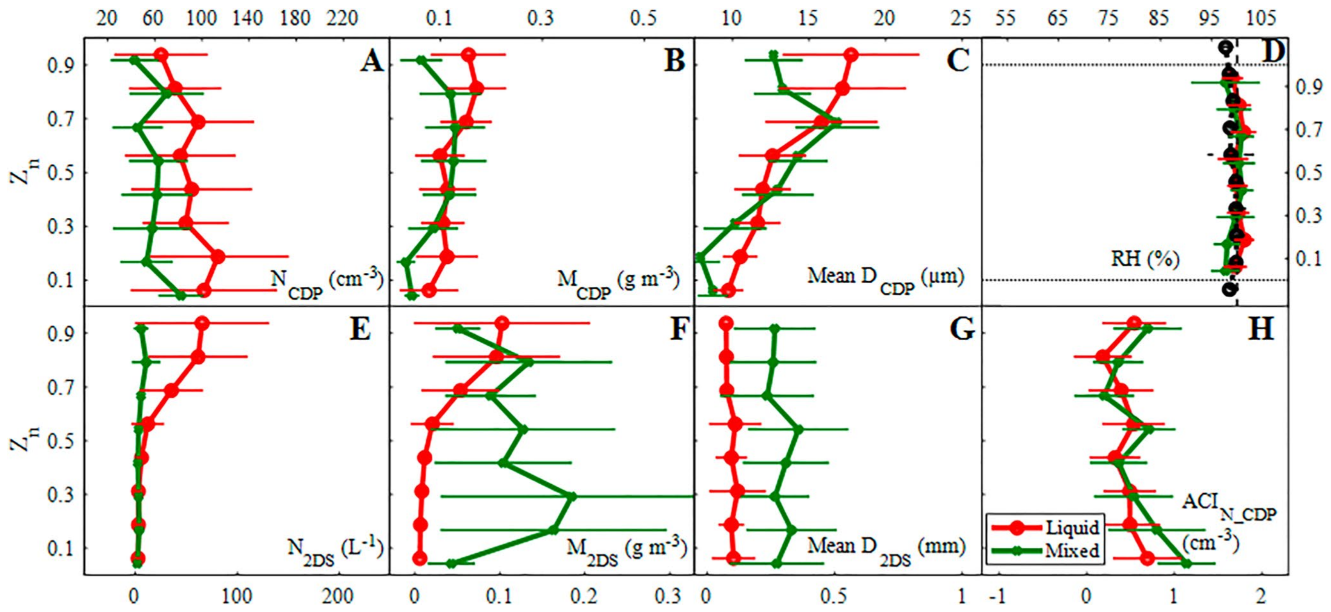

Figure 15. Similar to Figure 14 except for the lowest layer of multi-layer clouds.

with height and clear-sky RH above cloud top is nearly saturated (~96%) with little variance (standard deviation ~ 3%) for the lowest layer in the multi-layer clouds.

Figure 16 shows a similar analysis for the top cloud layers (Figures 16a–16d), the non-top cloud layers (Figures 16e–h), and middle layers (Figures 16i–16l) of multi-layer clouds. Average N_{CDP}, Mean D_{CDP}, N_{2DS} and RH are shown for the layer types. N_{CDP} increases with increasing height and peaks above $z_n = 0.5$ for top cloud layers, and below 0.5 for non-top layers. When removing single-layer clouds from the top cloud layer analysis, N_{CDP} similarly peaks above $z_n = 0.5$ (Figure S1 in Supporting Information S1). Mean D_{CDP} increases with height for all layer types. However, differences are observed in the overlying clear-sky RH for the top and non-top layers. Similar to the differences in single- and lowest multi-layer clouds (Figures 14d and 15d), the air is nearly saturated above non-top cloud layers while RH is only ~70% above top layers. When separately evaluating highest multi-layer clouds and removing single-layer clouds from the analysis, the overlying RH is ~90% (Figure S2 in Supporting Information S1). Differences in overlying RH may be expected as single-layer clouds will often be capped by rather strong inversions, whereas layers above one another will be associated with weaker inversions. In contrast, reduced longwave cooling at cloud top will be associated with underlying cloud layers of multi-layer regimes rather than top cloud layers.

4. Discussion

The results presented in Section 3 showed the dependence of cloud phase on relative cloud layer height, and on INP and CCN concentrations. There is a clear tendency for underlying cloud layers of multi-layer clouds to have greater frequencies of ice-containing samples, regardless of whether cloud layers were classified by the height relative to the lowest cloud layer or by bottom, middle and highest layers. The frequency of precipitating ice in-between cloud layers was examined to test whether its presence was associated with a prominent seeder-feeder mechanism. About 70% of precipitating samples in-between cloud layers contain ice (Figure 3d), and the large frequency of precipitating samples as well as nearly saturated samples within cloud layers (Figure 3c) is further evidence of a prominent seeder-feeder mechanism over the region.

The distribution and vertical structure of drop clustering was characterized to compare against previous studies that examined entrainment-mixing and its impacts based on drop size distribution inhomogeneities (Bower & Choularton, 1988; Paluch, 1986; Paluch & Knight, 1984). Entrainment-mixing is often characterized as homogeneous or inhomogeneous. Homogeneous mixing characteristically results in a shift of drop size distributions toward smaller drop sizes due to rapid mixing causing all droplets to experience partial evaporation, whereas

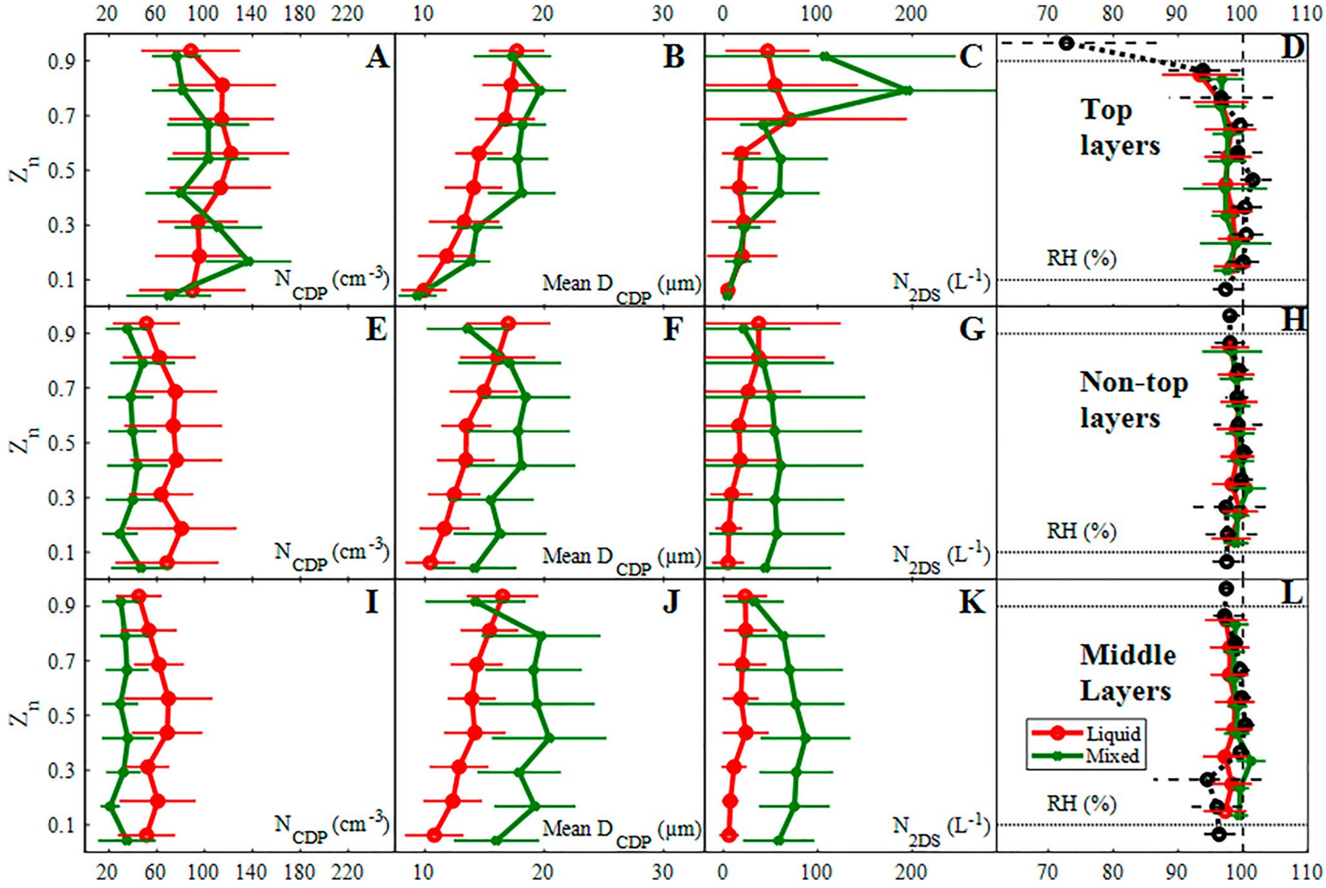

Figure 16. Similar to Figures 14 and 15 except results are shown for the top cloud layers (a–d), non-top cloud layers (e–h) and for all cloud layers enclosed within the lowest and highest cloud layers of multi-layer clouds (i–l). Unlike Figures 14 and 15, results here are only shown for N_{CDP} (a, e, and i), Mean D_{CDP} (b, f, and j), N_{2DS} (c, g, and k) and relative humidity (d, h, and l).

inhomogeneous mixing results in a reduction of droplet number concentrations but not in droplet sizes due to slower mixing causing different drops to experience different amounts of subsaturation (M. B. Baker et al., 1980; Latham & Reed, 1977). The latter pertains to *extreme* inhomogeneous mixing, whereas most mixing events do not necessarily follow one or the other extreme (e.g., Korolev et al., 2016).

Drop clustering was greater at cloud top of the highest cloud layers (including single layer clouds) compared with underlying layers, likely due to differences in entrainment and mixing strength between the different layer types. Lower clustering values at cloud top, as well as the lower variability of these values between cloud top ($z_n > 0.9$) and the cloud beneath ($z_n < 0.9$) for the underlying layers compared with the highest cloud layers (Figure 10), is consistent with weaker entrainment-mixing (potentially indicative of extreme inhomogeneous mixing) for underlying layers. It is important to note that clustering values are sensitive to the spatial scales used (e.g., B. A. Baker & Lawson, 2010) and can be computed in different ways, such as utilizing drop interarrival times to determine clustering values on smaller scales, of which further information can be found in Kostinski and Shaw (2001) and Shaw et al. (2002). The purpose of this study is to compare relative differences between cloud layer types, rather than provide an absolute measure of clustering. Clustering on the order of tens to a hundred meters (used here) has previously been directly correlated with entrainment and associated mixing (e.g., Dodson & Small Griswold, 2019; Small & Chuang, 2008).

The mixing of nearly saturated air would have a diminished impact on drop populations compared with considerably subsaturated air. Namely, the mixing of drier air likely results in local pockets of evaporation on relatively large spatial-scales, which increases drop clustering (e.g., B. A. Baker, 1992). The drier air above cloud for top layers compared with non-top layers (Figures 16d and 16h) is consistent with greater cloud top clustering for the top layers. The saturated air overlying non-top cloud layers may be important, as previous modeling studies have shown the presence of humidity inversions are required to maintain low-level mixed phase clouds in the Arctic (Curry, 1986; Curry et al., 1988; Solomon et al., 2011). The saturated air could also be associated with evaporating drizzle or sublimating ice from overlying cloud layers. Following Pruppacher and Klett (1996) and Lamb and Verlinde (2011), a spherical ice particle ranging from $D = 50$ to 150 μm in environments having RH with respect to ice ranging from 60% to 80% at temperatures ranging from −20° to 0°C results in ice particles which can fall for distances ranging tens of meters to ~1.5 km before completely sublimating. In this study, cloud top observations less than 200 m from the overlying cloud layer account for 47% of the cases, and observations less than 1 km from the overlying cloud account for 86%, showing that seeding would be expected to have an impact.

Despite differences in above cloud RH as well as cloud top clustering and cooling rates for top and non-top layers, droplets greater than 50 μm are observed at cloud top of all layer types with average concentrations ranging from ~20 to 50 L^{-1} (Figures 16c and 16g). Other factors may contribute to the common occurrence of droplet diameters exceeding 50 μm, such as sea salt acting as giant CCN (e.g., CCN with maximum dimensions exceeding 2 μm; Jensen & Nugent, 2017). Additionally, mean D_{2DS} generally increases from cloud top toward cloud base (Figures 14g and 15g), suggesting collision-coalescence may begin near cloud top.

5. Conclusions

The microphysical properties of single- and multi-layer clouds over the Southern Ocean were evaluated and contrasted using airborne in situ observations acquired during SOCRATES. Cloud layers were classified using a novel smoothing method applied to in-situ cloud observations acquired during sawtooths of the aircraft. This resulted in 55 profiles of single-layer clouds and 183 profiles of individual multi-layer clouds. Single-layer clouds have greater cloud liquid droplet mass and number concentrations than multi-layer clouds, with number concentrations in single-layer clouds from two research flights in coupled environments approximately double those in decoupled environments. Multi-layer clouds have broader drop size distributions than single-layer clouds. When cloud layers are separated according to whether they are underlying other cloud layers (non-top cloud layers) or not (top cloud layers), non-top cloud layers have broader drop size distributions ($D < 50$ μm) and total particle size distributions throughout the vertical cloud depth compared to top cloud layers.

The liquid phase most frequently occurs in single-layer clouds compared with multi-layer clouds. Liquid phase frequencies in multi-layer clouds are the lowest in the lowest cloud layers and increase with higher cloud layers until the third highest layer is reached, suggesting a prominent seeder-feeder presence in multi-layer clouds (Figure 2b). When classifying the layers of multi-layer clouds as lowest, highest, and those lying in-between, the highest cloud layers have the greatest frequency of liquid phase samples, and the middle layers have similarly low relative frequencies as the lowest layers (Figure 13b). These findings show that caution should be taken when quantifying cloud phase frequencies solely from satellite imagery due to potential biases in cloud top phase as well as overlapping cloud layers, as well as caution in classifying phase frequency by temperature alone.

Relative phase frequencies are also explored in relation to CCN and INP concentrations. There is some evidence of INP concentrations being positively related to ice frequencies (e.g., a correlation of −0.41 is observed for INP with activation temperatures from −30° to −10°C and liquid phase frequencies from −20° to −2°C in the boundary layer), but it is only observed for select temperature and INP activation temperature ranges (Figure 4). The lack of a relation for other temperature and activation temperatures suggests alternative processes, such as secondary ice production and accretion, play a major role in phase determination. Phase frequencies are found to be directly related to CCN concentrations, but only above the boundary layer and primarily at temperatures less than −10°C (Figure 5). Namely, ice is less likely to be observed in such environments with high CCN concentrations.

The dependence of cloud microphysical properties on cloud layer normalized height was also examined. The number weighted mean diameter of drops less than 50 μm increases with height for all cloud layer types, whereas number concentrations peak near cloud top for top cloud layers and near cloud base for non-top cloud layers (Figure 12). The number concentration and mass of drops greater than 50 μm also increase with cloud height, whereas the mean diameter decreases with increasing height. These similarities are observed between single- and multi-layer clouds in spite of differences in cloud top droplet clustering, radiative cooling profiles, overlying RH and relative phase frequencies, highlighting a propensity for precipitation initiation in both single and multi-layer clouds. However, robust differences in the microphysical properties of single- and multi-layer clouds warrants further investigation to distinguish and constrain physical responses resulting in the differences provide here.

Data Availability Statement

The data were collected using NSF's Lower Atmosphere Observing Facilities, which are managed and operated by NCAR's Earth Observing Laboratory. The NSF SOCRATES campaign data set is publicly available and can be accessed at http://www.eol.ucar.edu/field_projects/socrates. Data includes 2DS particle size distributions (Wu & McFarquhar, 2019), raw 2DS particle imagery (NCAR/EOL, 2018) and alternative in situ instrumentation (NCAR/EOL, 2022).

Acknowledgments
This work was supported by the National Science Foundation (NSF) through Grants AGS-1628674, AGS-160486 and AGS-1762096. This material is based upon work supported by the National Center for Atmospheric Research, which is a major facility sponsored by the National Science Foundation under Cooperative Agreement No. 1852977. The data were collected using NSF's Lower Atmosphere Observing Facilities, which are managed and operated by NCAR's Earth Observing Laboratory. The NSF SOCRATES campaign data set is publicly available and can be accessed at http://www.eol.ucar.edu/field_projects/socrates. We thank the pilots, mechanics, technicians, scientists, software engineers, and project managers of the NCAR EOL Research Aviation Facility for their support in the field and in post-processing data. We would like to thank the Australian Bureau of Meteorology Tasmanian regional Office for the excellent forecast support and weather briefings provided during the field campaign with special thanks to Scott Carpentier, Michelle Hollister, Matthew Thomas and Robert Schaap.

References

Ahn, E., Huang, Y., Chubb, T. H., Baumgardner, D., Isaac, P., de Hoog, M., et al. (2017). In situ observations of wintertime low-altitude clouds over the Southern Ocean. *Quarterly Journal of the Royal Meteorological Society*, *143*(704), 1381–1394. https://doi.org/10.1002/qj.3011

Ahn, E., Huang, Y., Siems, S. T., & Manton, M. J. (2018). A comparison of cloud microphysical properties derived from MODIS and CALIPSO with in situ measurements over the wintertime Southern Ocean. *Journal of Geophysical Research: Atmospheres*, *123*(19), 11120–11140. https://doi.org/10.1029/2018JD028535

Alexander, S. P., McFarquhar, G. M., Marchand, R., Protat, A., Vignon, É., Mace, G. G., & Klekociuk, A. R. (2021). Mixed-phase clouds and precipitation in Southern Ocean cyclones and cloud systems observed poleward of 64°S by ship-based cloud radar and lidar. *Journal of Geophysical Research: Atmospheres*, *126*(8), e2020JD033626. https://doi.org/10.1029/2020JD033626

Atlas, R. L., Bretherton, C. S., Blossey, P. N., Gettelman, A., Bardeen, C., Lin, P., & Ming, Y. (2020). How well do large-Eddy simulations and global climate models represent observed boundary layer structures and low clouds over the summertime Southern Ocean? *Journal of Advances in Modeling Earth Systems*, *12*(11), e2020MS002205. https://doi.org/10.1029/2020MS002205

Baker, B. A. (1992). Turbulent entrainment and mixing in clouds: A new observational approach. *Journal of the Atmospheric Sciences*, *49*(5), 387–404. https://doi.org/10.1175/1520-0469(1992)049<0387:TEAMIC>2.0.CO;2

Baker, B. A., & Lawson, R. P. (2010). Analysis of tools used to quantify droplet clustering in clouds. *Journal of the Atmospheric Sciences*, *67*(10), 3355–3367. https://doi.org/10.1175/2010JAS3409.1

Baker, M. B., Corbin, R. G., & Latham, J. (1980). The influence of entrainment on the evolution of cloud droplet spectra: I. A model of inhomogeneous mixing. *Quarterly Journal of the Royal Meteorological Society*, *106*(449), 581–598. https://doi.org/10.1002/qj.49710644914

Baumgardner, D., & Korolev, A. (1997). Airspeed corrections for optical array probe sample volumes. *Journal of Atmospheric and Oceanic Technology*, *14*(5), 1224–1229. https://doi.org/10.1175/1520-0426(1997)014<1224:ACFOAP>2.0.CO;2

Bodas-Salcedo, A., Hill, P. G., Furtado, K., Williams, K. D., Field, P. R., Manners, J. C., et al. (2016). Large contribution of supercooled liquid clouds to the solar radiation budget of the Southern Ocean. *Journal of Climate*, *29*(11), 4213–4228. https://doi.org/10.1175/JCLI-D-15-0564.1

Boers, R., Jensen, J. B., & Krummel, P. B. (1998). Microphysical and short-wave radiative structure of stratocumulus clouds over the Southern Ocean: Summer results and seasonal differences. *Quarterly Journal of the Royal Meteorological Society*, *124*(545), 151–168. https://doi.org/10.1002/qj.49712454507

Boers, R., Jensen, J. B., Krummel, P. B., & Gerber, H. (1996). Microphysical and short-wave radiative structure of wintertime stratocumulus clouds over the Southern Ocean. *Quarterly Journal of the Royal Meteorological Society*, *122*(534), 1307–1339. https://doi.org/10.1002/qj.49712253405

Bower, K. N., & Choularton, T. W. (1988). The effects of entrainment on the growth of droplets in continental cumulus clouds. *Quarterly Journal of the Royal Meteorological Society*, *114*(484), 1411–1434. https://doi.org/10.1002/qj.49711448404

Braslau, N., & Dave, J. V. (1975). Atmospheric heating rates due to solar radiation for several aerosol-Laden cloudy and cloud-free models. *Journal of Applied Meteorology*, *14*(3), 396–399. https://doi.org/10.1175/1520-0450(1975)014<0396:ahrdts>2.0.co;2

Chaumat, L., & Brenguier, J. L. (2001). Droplet spectra broadening in cumulus clouds. Part II: Microscale droplet concentration heterogeneities. *Journal of the Atmospheric Sciences*, *58*(6), 642–654. https://doi.org/10.1175/1520-0469(2001)058<0642:DSBICC>2.0.CO;2

Christensen, M. W., Carrió, G. G., Stephens, G. L., & Cotton, W. R. (2013). Radiative impacts of free-tropospheric clouds on the properties of marine stratocumulus. *Journal of the Atmospheric Sciences*, *70*(10), 3102–3118. https://doi.org/10.1175/JAS-D-12-0287.1

Chubb, T. H., Huang, Y., Jensen, J., Campos, T., Siems, S., & Manton, M. (2016). Observations of high droplet number concentrations in Southern Ocean boundary layer clouds. *Atmospheric Chemistry and Physics*, *16*(2), 971–987. https://doi.org/10.5194/acp-16-971-2016

Chubb, T. H., Jensen, J. B., Siems, S. T., & Manton, M. J. (2013). In situ observations of supercooled liquid clouds over the Southern Ocean during the HIAPER Pole-to-Pole Observation campaigns. *Geophysical Research Letters*, *40*(19), 5280–5285. https://doi.org/10.1002/grl.50986

Collins, W. D. (2001). Parameterization of generalized cloud overlap for radiative calculations in general circulation models. *Journal of the Atmospheric Sciences*, *58*(21), 3224–3242. https://doi.org/10.1175/1520-0469(2001)058<3224:POGCOF>2.0.CO;2

Cooper, W. A., Friesen, R. B., Hayman, M., Jensen, J. B., Lenschow, D. H., Romashkin, P. A., et al. (2016). Characterization of uncertainty in measurements of wind from the NSF/NCAR Gulfstream V research aircraft. Retrieved from https://opensky.ucar.edu/islandora/object/technotes%3A540/datastream/PDF/download/Characterization_of_Uncertainty_in_Measurements_of_Wind_from_the_NSF_NCAR_Gulfstream_V_Research_Aircraft.citation

Coopman, Q., Riedi, J., Zeng, S., & Garrett, T. J. (2020). Space-based analysis of the cloud thermodynamic phase transition for varying microphysical and meteorological regimes. *Geophysical Research Letters*, *47*(6), e2020GL087122. https://doi.org/10.1029/2020GL087122

Curry, J. A. (1986). Interactions among turbulence, radiation and microphysics in Arctic stratus clouds. *Journal of the Atmospheric Sciences*, *43*(1), 90–106. https://doi.org/10.1175/1520-0469(1986)043<0090:IATRAM>2.0.CO;2

Curry, J. A., Ebert, E. E., & Herman, G. F. (1988). Mean and turbulence structure of the summertime Arctic cloudy boundary layer. *Quarterly Journal of the Royal Meteorological Society*, *114*(481), 715–746. https://doi.org/10.1002/qj.49711448109

D'Alessandro, J. J., Diao, M., Wu, C., Liu, X., Jensen, J. B., & Stephens, B. B. (2019). Cloud phase and relative humidity distributions over the Southern Ocean in austral summer based on in situ observations and CAM5 simulations. *Journal of Climate*, *32*(10), 2781–2805. https://doi.org/10.1175/JCLI-D-18-0232.1

D'Alessandro, J. J., McFarquhar, G. M., Wu, W., Stith, J. L., Jensen, J. B., & Rauber, R. M. (2021). Characterizing the occurrence and spatial heterogeneity of liquid, ice, and mixed phase low-level clouds over the Southern Ocean using in situ observations acquired during SOCRATES. *Journal of Geophysical Research: Atmospheres*, *126*(11), e2020JD034482. https://doi.org/10.1029/2020JD034482

DeMott, P. J., Hill, T. C. J., Petters, M. D., Bertram, A. K., Tobo, Y., Mason, R. H., et al. (2017). Comparative measurements of ambient atmospheric concentrations of ice nucleating particles using multiple immersion freezing methods and a continuous flow diffusion chamber. *Atmospheric Chemistry and Physics*, *17*(18), 11227–11245. https://doi.org/10.5194/acp-17-11227-2017

Diao, M. (2021). VCSEL 1 Hz water vapor data: UCAR/NCAR—Earth Observing Laboratory. Retrieved from https://data.eol.ucar.edu/dataset/552.051

Dodson, D. S., & Small Griswold, J. D. (2019). Droplet inhomogeneity in shallow cumuli: The effects of in-cloud location and aerosol number concentration. *Atmospheric Chemistry and Physics*, *19*(11), 7297–7317. https://doi.org/10.5194/acp-19-7297-2019

Eloranta, E. E. (2006). High spectral resolution lidar. In *Lidar* (pp. 143–163). Springer-Verlag. https://doi.org/10.1007/0-387-25101-4_5

Engeln, A. V., & Teixeira, J. (2013). A planetary boundary layer height climatology derived from ECMWF reanalysis data. *Journal of Climate*, *26*(17), 6575–6590. https://doi.org/10.1175/JCLI-D-12-00385.1

Fiddes, S. L., Protat, A., Mallet, M. D., Alexander, S. P., & Woodhouse, M. T. (2022). Southern Ocean cloud and shortwave radiation biases in a nudged climate model simulation: Does the model ever get it right? Retrieved from https://acp.copernicus.org/preprints/acp-2022-259/

Field, P. R., Heymsfield, A. J., & Bansemer, A. (2006). Shattering and particle interarrival times measured by optical array probes in ice clouds. *Journal of Atmospheric and Oceanic Technology*, *23*(10), 1357–1371. https://doi.org/10.1175/JTECH1922.1

Field, P. R., Wood, R., Brown, P. R. A., Kaye, P. H., Hirst, E., Greenaway, R., & Smith, J. A. (2003). Ice particle interarrival times measured with a fast FSSP. *Journal of Atmospheric and Oceanic Technology*, *20*(2), 249–261. https://doi.org/10.1175/1520-0426(2003)020<0249:IPITMW>2.0.CO;2

Filioglou, M., Mielonen, T., Balis, D., Giannakaki, E., Arola, A., Kokkola, H., et al. (2019). Aerosol effect on the cloud phase of low-level clouds over the Arctic. *Journal of Geophysical Research: Atmospheres*, *124*(14), 7886–7899. https://doi.org/10.1029/2018JD030088

Finlon, J. A., McFarquhar, G. M., Nesbitt, S. W., Rauber, R. M., Morrison, H., Wu, W., & Zhang, P. (2019). A novel approach for characterizing the variability in mass–dimension relationships: Results from MC3E. *Atmospheric Chemistry and Physics*, *19*(6), 3621–3643. https://doi.org/10.5194/acp-19-3621-2019

Finlon, J. A., Rauber, R. M., Wu, W., Zaremba, T. J., McFarquhar, G. M., Nesbitt, S. W., et al. (2020). Structure of an atmospheric river over Australia and the Southern Ocean: II. Microphysical evolution. *Journal of Geophysical Research: Atmospheres*, *125*(18). https://doi.org/10.1029/2020JD032514

Fleishauer, R. P., Larson, V. E., & Vonder Haar, T. H. (2002). Observed microphysical structure of midlevel, mixed-phase clouds. *Journal of the Atmospheric Sciences*, *59*(11), 1779–1804. https://doi.org/10.1175/1520-0469(2002)059<1779:OMSOMM>2.0.CO;2

Gettelman, A., Bardeen, C. G., McCluskey, C. S., Järvinen, E., Stith, J., Bretherton, C., et al. (2020). Simulating observations of Southern Ocean clouds and implications for climate. *Journal of Geophysical Research: Atmospheres*, *125*(21), e2020JD032619. https://doi.org/10.1029/2020JD032619

Hallett, J., & Mossop, S. C. (1974). Production of secondary ice particles during the riming process. *Nature*, *249*(5452), 26–28. https://doi.org/10.1038/249026a0

Hande, L. B., Siems, S. T., Manton, M. J., & Belusic, D. (2012). Observations of wind shear over the Southern Ocean. *Journal of Geophysical Research*, *117*(D12). https://doi.org/10.1029/2012JD017488

Haynes, J. M., Jakob, C., Rossow, W. B., Tselioudis, G., & Brown, J. B. (2011). Major characteristics of Southern Ocean cloud regimes and their effects on the energy budget. *Journal of Climate*, *24*(19), 5061–5080. https://doi.org/10.1175/2011JCLI4052.1

Herman, G., & Goody, R. (1976). Formation and persistence of summertime arctic stratus clouds. *Journal of the Atmospheric Sciences*, *33*(8), 1537–1553. https://doi.org/10.1175/1520-0469(1976)033<1537:FAPOSA>2.0.CO;2

Heymsfield, A. J., Field, P. R., Bailey, M., Rogers, D., Stith, J., Twohy, C., et al. (2011). Ice in clouds experiment-layer clouds. Part I: Ice growth rates derived from lenticular wave cloud penetrations. *Journal of the Atmospheric Sciences*, *68*(11), 2628–2654. https://doi.org/10.1175/JAS-D-11-025.1

Heymsfield, A. J., & Parrish, J. L. (1978). Computation technique for increasing the effective sampling volume of the PMS two-dimensional particle size spectrometer. *Journal of Applied Meteorology*, *17*(10), 1566–1572. https://doi.org/10.1175/1520-0450(1978)017<1566:ACTFIT>2.0.CO;2

Hobbs, P. V., & Rangno, A. L. (1998). Microstructures of low and middle-level clouds over the Beaufort Sea. *Quarterly Journal of the Royal Meteorological Society*, *124*(550), 2035–2071. https://doi.org/10.1002/qj.49712455012

Holroyd, E. W. (1987). Some techniques and uses of 2D-C habit classification software for snow particles. *Journal of Atmospheric and Oceanic Technology*, *4*(3), 498–511. https://doi.org/10.1175/1520-0426(1987)004<0498:stauoc>2.0.co;2

Houze, R. A. (2014). Cloud dynamics. In *International geophysics* (104, pp. 1–432). Academic Press. https://doi.org/10.1016/B978-0-12-374266-7.00001-9

Hu, Y., Winker, D., Vaughan, M., Lin, B., Omar, A., Trepte, C., et al. (2009). CALIPSO/CALIOP cloud phase discrimination algorithm. *Journal of Atmospheric and Oceanic Technology*, *26*(11), 2293–2309. https://doi.org/10.1175/2009JTECHA1280.1

Huang, Y., Franklin, C. N., Siems, S. T., Manton, M. J., Chubb, T., Lock, A., et al. (2015). Evaluation of boundary-layer cloud forecasts over the Southern Ocean in a limited-area numerical weather prediction system using in situ, space-borne and ground-based observations. *Quarterly Journal of the Royal Meteorological Society*, *141*(691), 2259–2276. https://doi.org/10.1002/qj.2519

Huang, Y., Siems, S. T., & Manton, M. J. (2021). Wintertime in situ cloud microphysical properties of mixed-phase clouds over the Southern Ocean. *Journal of Geophysical Research: Atmospheres*, *126*(11), e2021JD034832. https://doi.org/10.1029/2021JD034832

Huang, Y., Siems, S. T., Manton, M. J., & Thompson, G. (2014). An evaluation of WRF simulations of clouds over the Southern Ocean with A-train observations. *Monthly Weather Review*, *142*(2), 647–667. https://doi.org/10.1175/MWR-D-13-00128.1

Hudson, J. G., & Frisbie, P. R. (1991). Cloud condensation nuclei near marine stratus. *Journal of Geophysical Research*, *96*(D11), 20795–20808. https://doi.org/10.1029/91jd02212

Intrieri, J. M., Shupe, M. D., Uttal, T., & McCarty, B. J. (2002). An annual cycle of Arctic cloud characteristics observed by radar and lidar at SHEBA. *Journal of Geophysical Research*, *107*(10), SHE 5-1. https://doi.org/10.1029/2000jc000423

Jackson, R. C., McFarquhar, G. M., Korolev, A. V., Earle, M. E., Liu, P. S. K., Lawson, R. P., et al. (2012). The dependence of ice microphysics on aerosol concentration in arctic mixed-phase stratus clouds during ISDAC and M-PACE. *Journal of Geophysical Research*, *117*(15). https://doi.org/10.1029/2012JD017668

Jackson, R. C., Mcfarquhar, G. M., Stith, J., Beals, M., Shaw, R. A., Jensen, J., et al. (2014). An assessment of the impact of antishattering tips and artifact removal techniques on cloud ice size distributions measured by the 2D cloud probe. *Journal of Atmospheric and Oceanic Technology*, *31*(12), 2567–2590. https://doi.org/10.1175/JTECH-D-13-00239.1

Jaczewski, A., & Malinowski, S. P. (2005). Spatial distribution of cloud droplets in a turbulent cloud-chamber flow. *Quarterly Journal of the Royal Meteorological Society*, *131*(609), 2047–2062. https://doi.org/10.1256/qj.04.65

Järvinen, E., McCluskey, C. S., Waitz, F., Schnaiter, M., Bansemer, A., Bardeen, C. G., et al. (2022). Evidence for secondary ice production in Southern Ocean maritime boundary layer clouds. *Journal of Geophysical Research: Atmospheres*, *127*(16), e2021JD036411. https://doi.org/10.1029/2021jd036411

Jensen, J. B., & Nugent, A. D. (2017). Condensational growth of drops formed on giant sea-salt aerosol particles. *Journal of the Atmospheric Sciences*, *74*(3), 679–697. https://doi.org/10.1175/JAS-D-15-0370.1

Jiang, Q., & Wang, S. (2012). Impact of gravity waves on marine stratocumulus variability. *Journal of the Atmospheric Sciences*, *69*(12), 3633–3651. https://doi.org/10.1175/JAS-D-12-0135.1

Kay, J. E., Hillman, B. R., Klein, S. A., Zhang, Y., Medeiros, B., Pincus, R., et al. (2012). Exposing global cloud biases in the community atmosphere model (CAM) using satellite observations and their corresponding instrument simulators. *Journal of Climate*, *25*(15), 5190–5207. https://doi.org/10.1175/JCLI-D-11-00469.1

Khanal, S., & Wang, Z. (2018). Uncertainties in MODIS-based cloud liquid water path retrievals at high Latitudes due to mixed-phase clouds and cloud top height inhomogeneity. *Journal of Geophysical Research: Atmospheres*, *123*(19), 11154–11172. https://doi.org/10.1029/2018JD028558

Kim, S., & Casper, R. (2013). *Applications of convolution in image processing with MATLAB* (pp. 1–20). University of Washington.

Korolev, A., Khain, A., Pinsky, M., & French, J. (2016). Theoretical study of mixing in liquid clouds-Part 1: Classical concepts. *Atmospheric Chemistry and Physics*, *16*(14), 9235–9254. https://doi.org/10.5194/acp-16-9235-2016

Korolev, A., & Leisner, T. (2020). Review of experimental studies of secondary ice production. *Atmospheric Chemistry and Physics*, *20*(20), 11767–11797. https://doi.org/10.5194/acp-20-11767-2020

Kostinski, A. B., & Shaw, R. A. (2001). Scale-dependent droplet clustering in turbulent clouds. *Journal of Fluid Mechanics*, *434*, 389–398. https://doi.org/10.1017/S0022112001004001

Lamb, D., & Verlinde, J. (2011). *Physics and chemistry of clouds. Physics and chemistry of clouds*. Cambridge University Press. https://doi.org/10.1017/CBO9780511976377

Lance, S., Brock, C. A., Rogers, D., & Gordon, J. A. (2010). Water droplet calibration of the Cloud Droplet Probe (CDP) and in-flight performance in liquid, ice and mixed-phase clouds during ARCPAC. *Atmospheric Measurement Techniques*, *3*(6), 1683–1706. https://doi.org/10.5194/amt-3-1683-2010

Latham, J., & Reed, R. L. (1977). Laboratory studies of the effects of mixing on the evolution of cloud droplet spectra. *Quarterly Journal of the Royal Meteorological Society*, *103*(436), 297–306. https://doi.org/10.1002/qj.49710343607

Levin, E. J. T., DeMott, P. J., Suski, K. J., Boose, Y., Hill, T. C. J., McCluskey, C. S., et al. (2019). Characteristics of ice nucleating particles in and around California winter storms. *Journal of Geophysical Research: Atmospheres*, *124*(21), 11530–11551. https://doi.org/10.1029/2019JD030831

Li, J., Yi, Y., Minnis, P., Huang, J., Yan, H., Ma, Y., et al. (2011). Radiative effect differences between multi-layered and single-layer clouds derived from CERES, CALIPSO, and CloudSat data. *Journal of Quantitative Spectroscopy and Radiative Transfer*, *112*(2), 361–375. https://doi.org/10.1016/j.jqsrt.2010.10.006

Liu, Y., Key, J. R., Ackerman, S. A., Mace, G. G., & Zhang, Q. (2012). Arctic cloud macrophysical characteristics from CloudSat and CALIPSO. *Remote Sensing of Environment*, *124*, 159–173. https://doi.org/10.1016/j.rse.2012.05.006

Luo, Y., Xu, K.-M., Morrison, H., McFarquhar, G. M., Wang, Z., & Zhang, G. (2008). Multi-layer arctic mixed-phase clouds simulated by a cloud-resolving model: Comparison with ARM observations and sensitivity experiments. *Journal of Geophysical Research*, *113*(D12), D12208. https://doi.org/10.1029/2007JD009563

Matus, A. V., & L'Ecuyer, T. S. (2017). The role of cloud phase in Earth's radiation budget. *Journal of Geophysical Research: Atmospheres*, *122*(5), 2559–2578. https://doi.org/10.1002/2016JD025951

McCluskey, C. S., Hill, T. C. J., Humphries, R. S., Rauker, A. M., Moreau, S., Strutton, P. G., et al. (2018). Observations of ice nucleating particles over Southern Ocean waters. *Geophysical Research Letters*, *45*(21), 11989–11997. https://doi.org/10.1029/2018GL079981

McCoy, D. T., Hartmann, D. L., Grosvenor, D. P., McCoy, D. T., Hartmann, D. L., & Grosvenor, D. P. (2014). Observed Southern Ocean Cloud properties and shortwave reflection. Part I: Calculation of SW flux from observed cloud properties. *Journal of Climate*, *27*(23), 8836–8857. https://doi.org/10.1175/JCLI-D-14-00287.1

McCoy, I. L., Bretherton, C. S., Wood, R., Twohy, C. H., Gettelman, A., Bardeen, C. G., & Toohey, D. W. (2021). Influences of recent particle formation on Southern Ocean aerosol variability and low cloud properties. *Journal of Geophysical Research: Atmospheres*, *126*(8), e2020JD033529. https://doi.org/10.1029/2020JD033529

McFarquhar, G. M. (2004). The effect of raindrop clustering on collision-induced break-up of raindrops. *Quarterly Journal of the Royal Meteorological Society*, *130*(601), 2169–2190. https://doi.org/10.1256/qj.03.98

McFarquhar, G. M., Baumgardner, D., Bansemer, A., Abel, S. J., Crosier, J., French, J., et al. (2017). Processing of ice cloud in situ data collected by bulk water, scattering, and imaging probes: Fundamentals, uncertainties, and efforts toward consistency. *Meteorological Monographs*, *58*, 11.1–11.33. https://doi.org/10.1175/amsmonographs-d-16-0007.1

McFarquhar, G. M., Bretherton, C., Marchand, R., Protat, A., DeMott, P. J., Alexander, S. P., et al. (2021). Observations of clouds, aerosols, precipitation, and surface radiation over the Southern Ocean: An overview of CAPRICORN, MARCUS, MICRE and SOCRATES. *Bulletin of the American Meteorological Society*, *102*(4), E894–E928. https://doi.org/10.1175/bams-d-20-0132.1

McFarquhar, G. M., Finlon, J. A., Stechman, D. M., Wu, W., Jackson, R. M., & Freer, M. (2018). *University of Illinois/Oklahoma optical array probe (OAP) processing software. Version 3.1.4*. Zenodo.

McFarquhar, G. M., Zhang, G., Poellot, M. R., Kok, G. L., McCoy, R., Tooman, T., et al. (2007). Ice properties of single-layer stratocumulus during the mixed-phase arctic cloud experiment: 1. Observations. *Journal of Geophysical Research*, *112*(D24), D24201. https://doi.org/10.1029/2007JD008633

Mioche, G., Jourdan, O., Delanoë, J., Gourbeyre, C., Febvre, G., Dupuy, R., et al. (2017). Vertical distribution of microphysical properties of Arctic springtime low-level mixed-phase clouds over the Greenland and Norwegian seas. *Atmospheric Chemistry and Physics*, *17*(20), 12845–12869. https://doi.org/10.5194/acp-17-12845-2017

Mossop, S. C. (1956). Sublimation nuclei. *Proceedings of the Physical Society Section B*, *69*(2), 161–164. https://doi.org/10.1088/0370-1301/69/2/305

Murphy, D. M., & Koop, T. (2005). Review of the vapour pressures of ice and supercooled water for atmospheric applications. *Quarterly Journal of the Royal Meteorological Society*, *131*(608), 1539–1565. https://doi.org/10.1256/qj.04.94

Naud, C. M., Booth, J. F., & Del Genio, A. D. (2014). Evaluation of ERA-Interim and MERRA cloudiness in the southern ocean. *Journal of Climate*, *27*(5), 2109–2124. https://doi.org/10.1175/JCLI-D-13-00432.1

Paluch, I. R. (1986). Mixing and the cloud droplet size spectrum: Generalizations from the CCOPE data. *Journal of the Atmospheric Sciences*, *43*(18), 1984–1993. https://doi.org/10.1175/1520-0469(1986)043<1984:MATCDS>2.0.CO;2

Paluch, I. R., & Knight, C. A. (1984). Mixing and the evolution of cloud droplet size spectra in a vigorous continental cumulus. *Journal of the Atmospheric Sciences*, *41*(11), 1801–1815. https://doi.org/10.1175/1520-0469(1984)041<1801:MATEOC>2.0.CO;2

Petty, G. W., & Grant, W. (2006). *A first course in atmospheric radiation*. Sundog Pub. Retrieved from https://sundogpublishingstore.myshopify.com/products/a-first-course-in-atmospheric-radiation-g-w-petty

Pruppacher, H. R., & Klett, J. D. (1996). *Microphysics of clouds and precipitation*. Springer Netherlands.

Rahn, D. A., & Garreaud, R. (2010). Marine boundary layer over the subtropical southeast Pacific during VOCALS-REx-Part 1: Mean structure and diurnal cycle. *Atmospheric Chemistry and Physics*, *10*(10), 4491–4506. https://doi.org/10.5194/acp-10-4491-2010

Rauber, R. M., Hu, H., Dominguez, F., Nesbitt, S. W., McFarquhar, G. M., Zaremba, T. J., & Finlon, J. A. (2020). Structure of an atmospheric river over Australia and the Southern Ocean. Part I: Tropical and midlatitude water vapor fluxes. *Journal of Geophysical Research: Atmospheres*, *125*(18), e2020JD032513. https://doi.org/10.1029/2020JD032513

Riedi, J., Marchant, B., Platnick, S., Baum, B. A., Thieuleux, F., Oudard, C., et al. (2010). Cloud thermodynamic phase inferred from merged POLDER and MODIS data. *Atmospheric Chemistry and Physics*, *10*(23), 11851–11865. https://doi.org/10.5194/acp-10-11851-2010

Roberts, G. C., & Nenes, A. (2005). A continuous-flow streamwise thermal-gradient CCN chamber for atmospheric measurements. *Aerosol Science and Technology*, *39*(3), 206–221. https://doi.org/10.1080/027868290913988

Sanchez, K. J., Roberts, G. C., Saliba, G., Russell, L. M., Twohy, C., Reeves, M. J., et al. (2021). Measurement report: Cloud processes and the transport of biological emissions affect southern ocean particle and cloud condensation nuclei concentrations. *Atmospheric Chemistry and Physics*, *21*(5), 3427–3446. https://doi.org/10.5194/acp-21-3427-2021

Sanchez, K. J., Russell, L. M., Modini, R. L., Frossard, A. A., Ahlm, L., Corrigan, C. E., et al. (2016). Meteorological and aerosol effects on marine cloud microphysical properties. *Journal of Geophysical Research: Atmospheres*, *121*(8), 4142–4161. https://doi.org/10.1002/2015JD024595

Savitzky, A., & Golay, M. J. E. (1964). Smoothing and differentiation of data by simplified least squares procedures. *Analytical Chemistry*, *36*(8), 1627–1639. https://doi.org/10.1021/ac60214a047

Schima, J., McFarquhar, G., Romatschke, U., Vivekanandan, J., D'Alessandro, J., Haggerty, J., et al. (2022). Characterization of Southern Ocean boundary layer clouds using airborne radar, lidar, and in-situ cloud data: Results from SOCRATES. *Journal of Geophysical Research: Atmospheres*, *127*(21). https://doi.org/10.1029/2022jd037277

Seidel, D. J., Zhang, Y., Beljaars, A., Golaz, J.-C., Jacobson, A. R., & Medeiros, B. (2012). Climatology of the planetary boundary layer over the continental United States and Europe. *Journal of Geophysical Research*, *117*(D17). https://doi.org/10.1029/2012JD018143

Shaw, R. A., Kostinski, A. B., & Larsen, M. L. (2002). Towards quantifying droplet clustering in clouds. *Quarterly Journal of the Royal Meteorological Society*, *128*(582), 1043–1057. https://doi.org/10.1256/003590002320373193

Shaw, R. A., Reade, W. C., Collins, L. R., & Verlinde, J. (1998). Preferential concentration of cloud droplets by turbulence: Effects on the early evolution of cumulus cloud droplet spectra. *Journal of the Atmospheric Sciences*, *55*(11), 1965–1976. https://doi.org/10.1175/1520-0469(1998)055<1965:PCOCDB>2.0.CO;2

Small, J. D., & Chuang, P. Y. (2008). New observations of precipitation initiation in warm cumulus clouds. *Journal of the Atmospheric Sciences*, *65*(9), 2972–2982. https://doi.org/10.1175/2008JAS2600.1

Solomon, A., Shupe, M. D., Persson, P. O. G., & Morrison, H. (2011). Moisture and dynamical interactions maintaining decoupled Arctic mixed-phase stratocumulus in the presence of a humidity inversion. *Atmospheric Chemistry and Physics*, *11*(19), 10127–10148. https://doi.org/10.5194/acp-11-10127-2011

Stith, J. L., Ramanathan, V., Cooper, W. A., Roberts, G. C., DeMott, P. J., Carmichael, G., et al. (2009). An overview of aircraft observations from the Pacific Dust Experiment campaign. *Journal of Geophysical Research*, *114*(D5), D05207. https://doi.org/10.1029/2008JD010924

Trenberth, K. E., & Fasullo, J. T. (2010). Simulation of present-day and twenty-first-century energy budgets of the southern oceans. *Journal of Climate*, *23*(2), 440–454. https://doi.org/10.1175/2009JCLI3152.1

Tsay, S. C., & Jayaweera, K. (1984). Physical characteristics of Arctic stratus clouds. *Journal of Climate and Applied Meteorology*, *23*(4), 584–596. https://doi.org/10.1175/1520-0450(1984)023<0584:PCOASC>2.0.CO;2

Twohy, C. H., McMeeking, G. R., DeMott, P. J., McCluskey, C. S., Hill, T. C. J., Burrows, S. M., et al. (2016). Abundance of fluorescent biological aerosol particles at temperatures conducive to the formation of mixed-phase and cirrus clouds. *Atmospheric Chemistry and Physics*, *16*(13), 8205–8225. https://doi.org/10.5194/acp-16-8205-2016

UCAR/NCAR—Earth Observing Laboratory. (2018). NSF/NCAR GV HIAPER raw 2D-S imagery. Version 1.0. [Dataset]. UCAR/NCAREarth. https://doi.org/10.26023/8HMG-WQP3-XA0X

UCAR/NCAR—Earth Observing Laboratory. (2022). SOCRATES: Low rate (LRT - 1 sps) navigation, state parameter, and microphysics flight-level data. Version 1.4. [Dataset]. UCAR/NCAREarth. https://doi.org/10.5065/D6M32TM9

Verlinde, J., Rambukkange, M. P., Clothiaux, E. E., McFarquhar, G. M., & Eloranta, E. W. (2013). Arctic multilayered, mixed-phase cloud processes revealed in millimeter-wave cloud radar Doppler spectra. *Journal of Geophysical Research: Atmospheres*, *118*(23), 13199–13213. https://doi.org/10.1002/2013JD020183

Vivekanandan, J., Ellis, S., Tsai, P., Loew, E., Lee, W. C., Emmett, J., et al. (2015). A wing pod-based millimeter wavelength airborne cloud radar A wing pod-based millimeter wavelength airborne cloud radar A wing pod-based millimeter wavelength airborne cloud radar. *Geoscientific Instrumentation, Methods and Data Systems*, *5*, 117–159. https://doi.org/10.5194/gid-5-117-2015

Vogelezang, D. H. P., & Holtslag, A. A. M. (1996). Evaluation and model impacts of alternative boundary-layer height formulations. *Boundary-Layer Meteorology*, *81*(3), 245–269. https://doi.org/10.1007/BF02430331

Wang, Y., McFarquhar, G. M., Rauber, R. M., Zhao, C., Wu, W., Finlon, J. A., et al. (2020). Microphysical properties of generating cells over the Southern Ocean: Results from SOCRATES. *Journal of Geophysical Research: Atmospheres*, *125*(13). https://doi.org/10.1029/2019JD032237

Wang, Z., Mora Ramirez, M., Dadashazar, H., MacDonald, A. B., Crosbie, E., Bates, K. H., et al. (2016). Contrasting cloud composition between coupled and decoupled marine boundary layer clouds. *Journal of Geophysical Research: Atmospheres*, *121*(19), 11679–11691. https://doi.org/10.1002/2016JD025695

Wu, W., & McFarquhar, G. M. (2019). NSF/NCAR GV Hiaper fast 2DS particle size distribution (PSD) product data. Version 1.1. [Dataset]. UCAR/NCAR-Earth Observing Laboratory. https://doi.org/10.26023/8hmg-wqp3-xa0x

Yang, C. A., Diao, M., Gettelman, A., Zhang, K., Sun, J., McFarquhar, G., & Wu, W. (2021). Ice and supercooled liquid water distributions over the Southern Ocean based on in situ observations and climate model simulations. *Journal of Geophysical Research: Atmospheres*, *126*(24), e2021JD036045. https://doi.org/10.1029/2021JD036045

Zondlo, M. A., Paige, M. E., Massick, S. M., & Silver, J. A. (2010). Vertical cavity laser hygrometer for the National science Foundation Gulfstream-V aircraft. *Journal of Geophysical Research*, *115*(D20), D20309. https://doi.org/10.1029/2010JD014445